Development of an Actively-Cooled Imaging System for Embedded Optical Measurements in High-Speed Flows

by

Ryan Alles

A thesis submitted to the Graduate Faculty of
Auburn University
in partial fulfillment of the
requirements for the Degree of
Master of Science

Auburn, Alabama
December 9, 2023

Keywords: optical diagnostics, experimental analysis, active cooling, thermal management

Copyright 2023 by Ryan Alles

Approved by

Brian Thurow, Department Chair, W. Allen and Martha Reed Professor
David Scarborough, Associate Professor of Aerospace Engineering
Michael Hamilton, James B. Davis Professor of Electrical and Computer Engineering

Abstract

High speed airbreathing propulsion systems have become increasingly complex with the development of hypersonic scramjet engines. Analysis of scramjet flow structures is difficult due to extreme thermal environments and limited optical access to internal flow paths. This study introduces an innovative actively-cooled miniature imaging system designed to broaden the applications of low-cost, small form factor image sensors for integration into extreme thermal environments, facilitating the observation of high-enthalpy flows.

The developed system enables non-intrusive optical flow field measurements in confined flows where traditional imaging systems have limited optical access. The design incorporates a cooled image sensor housing that actively cools the image sensor and lens assembly by immersing them in a dielectric cooling liquid, Fluorinert FC-72. The internal geometry of the housing facilitates the flow of the dielectric coolant, effectively regulating the thermal environment around the entire sensor package. A thermal management system regulates the thermal environment inside of the enclosed housing to protect the image sensor. A closed-loop cooling system continuously supplies fresh coolant to regulate hardware temperatures.

Experimental analysis demonstrated the actively-cooled miniature imaging system's capability to maintain the thermal environment of an image sensor at 100°F during extended exposure to 1,450°F, simulating a high-temperature flow path. This validates the system's ability to capture images in high-temperature supersonic flows, laying the groundwork for potential applications in high-enthalpy supersonic test facilities. Implementation of optical bandpass filters in the system design allows the system to capture chemiluminescence emissions produced by radicals in a methane flame, verifying the system's ability to generate spectrally-resolved images consistent with traditional image-based diagnostics of reacting flows.

This actively-cooled miniature imaging system offers a novel solution for internal flow measurements in high enthalpy flows, employing dielectric immersion cooling and cost-effective hardware components to observe regions that have been traditionally challenging to observe and measure. With further development, this system has the potential to be adapted as an inexpensive, lightweight, economical tool to obtain images during flight experiments in demanding thermal environments.

Acknowledgments

The work presented in this thesis could not have been completed without the knowledge and support provided by many people I have interacted with on this research journey. First, I would like to thank my advising professor and committee chair, Dr. Brian Thurow, for enabling me through his classroom teachings as well as providing beneficial feedback during my research process. I would also like to thank my co-researchers: Christopher Lewis and Griffin Eagan. Chris has significantly impacted this work by applying his knowledge of electronic design to implement the data collection and processing system. Chris also performed an extensive diagnosis (detailed in Chapter 4) to determine the limitations of the image sensor used in this work. Griffin's previous work provided the foundation for this current work. He also shared ample hands-on experience and information that cannot simply be acquired from classroom teachings. I would like to thank Dr. Brian Rice and his group at Air Force Research Laboratory for providing the opportunity to conduct this research through their support and guidance. I would like to thank our machinist, Andy Weldon, for sharing his knowledge and experience of standard machining practices as well as supporting this project by manufacturing all of the housing components. I would like to thank Dr. Michael Hamilton for providing support and feedback from his experience working with thermal management as the director of the Alabama Micro/Nano Science and Technology Center, as well as serving on my committee. I would like to thank Dr. David Scarborough for providing relevant classroom knowledge, as well as his willingness to serve on my committee. I thank all of the members of the Advanced Flow Diagnostics Laboratory for providing friendship and engaging in technical discussions. I would like to thank Dr. Eldon Triggs for providing support throughout my undergraduate career, helping build my passion

for applied aerospace engineering through guidance and encouragement to the Auburn University Rocketry Association. Lastly, I would like to thank my parents for their love and encouragement throughout my higher-education to help keep me focused on my studies and complete my work.

Table of Contents

List of Figures

List of Abbreviations

ACMIS actively-cooled miniature imaging system

ADC analog-to-digital conversion

AEDC Arnold Engineering Development Complex

CISH cooled image sensor housing

CLCS closed-loop cooling system

CMOS complementary metal-oxide semiconductor

COTS commercially-available, off-the-shelf

DCPS Data Collection and Processing System

FoV field of view

fps frames per second

FTSI fluid-thermal-structure interactions

IR infrared

MIPI mobile industry processor interface

MP megapixel

OFV oil flow visualization

PCB printed circuit board

PFIB perfluoroisobutylene

PSP pressure-sensitive paint

RC-19 Research Cell 19

RC-19 Research Cell 19

SBLI shock wave/boundary layer interactions

SDS safety data sheet

SNR signal-to-noise ratio

Chapter 1

Introduction

High speed flows are intriguing to scientists and researchers due to the complex phenomena that occur when travelling at speeds above the speed of sound, especially concerning hypersonic flows that can generate large amounts of heat on surfaces of an aircraft. These phenomena have implications in many technological domains, from supersonic aircraft design to space launch vehicle propulsion optimization. In the world today, researchers are competing to pushing the envelope of high-speed air-breathing propulsion systems to develop aircraft capable of hypersonic flight, especially regarding military applications where a vessel may need to reach a target without being intercepted. Novel high-speed air-breathing systems are developed through a combination of prototype testing and characterization of new component designs as well as diagnosis of shortcomings with existing systems.

Hypersonic component design and integration presents challenges due to the extreme environmental conditions experienced during flight and during ground tests in wind tunnel facilities. Characterization of these components presents additional challenges due to limitations with integration of traditional sensor technologies into crucial measurement regions that may be hard to instrument due to geometric constraints and environmental considerations. High temperatures, pressures, vibrations, and hardware operational safety must all be accounted for in the packaging and integration of hardware into a flight vehicle. One of the hardest challenges with hypersonic vehicle design is regional heating that can reach temperatures in the range of 3000°F to 5000°F [15–17]. This presents issues for hardware thermal regulation due to the extreme amount of heat that needs to be redirected away from sensitive measurement equipment. Hardware form factor must also be considered due to the low cross-sectional profile of modern hypersonic aircraft and the small scale of hypersonic

wind tunnel facilities. This makes it difficult to thermally regulate delicate sensor equipment being directly exposed to harsh environments.

Optical measurement techniques provide an ideal platform for high speed flow measurement because they can capture information about an entire region of a flow without disrupting the flow path. Unlike traditional probe hardware that are designed for a specific measurement, optical measurement data can be processed to reconstruct both transient and long term temporal information about a flow field, including velocity, pressure, temperature, and shock propagation. Optical measurements can be used to visualize flow structures and shock train propagation for model geometry validation using flow visualization techniques such as Schlieren [18–20], shadowgraph [20, 21], and surface oil flow visualization (OFV) [11, 20, 22, 23]. They can also be used to determine structural and thermal loadings from fluid-structure interactions using digital-image correlation [12] or to image combustion flame chemiluminescence [18, 21, 24–34] to determine combustor burn properties and characterize exhaust signatures. Due to harsh thermal environments produced during high speed experiments, scientific camera equipment is often positioned further away, requiring external space to observe some flows. This normally requires significant test article modification to gain optical access through transparent components to observe low-access regions and limits application of use with flight experiments.

Small form factor board-mounted CMOS image sensors can be used to expand the capabilities of optical measurement techniques in high-speed applications for viewing of confined flow regions that are not well understood. The low-cost and wide availability of these image sensors is convenient for experiments where short-term or even single-use systems may be necessary for disposable test articles or unrecoverable vehicle models. Board mounted image sensors have the potential to be embedded into confined geometries where optical measurements are difficult to perform with traditional imaging systems. This includes viewing of high-speed flows that can generate high enthalpy environments, making it difficult to provide optical access. Small board-mounted sensors have only been utilized for a handful of high

speed flow applications [11, 12, 22], making them a convenient platform to perform novel flow measurements.

This work expands the applications of board mounted image sensors by adapting the system from Eagan et al. [11] for use in harsh thermal environments. The described system is designed around geometric constraints and environmental conditions in the combustor flow path Supersonic Research Facility (RC-19) at Wright-Patterson Air Force Base. A board-mounted sensor is packaged in an enclosed housing to provide active cooling directly to the sensor and regulate its thermal environment. By cooling the entire imaging package and lens, the sensor can be positioned directly against harsh flow environments, providing a low-cost solution for optical diagnostics in high speed flows that can be embedded directly into test articles. Thermal experiments were conducted to simulate the conditions that would be experienced in the RC-19 combustor. Chemiluminescence imaging experiments were conducted to evaluate the system's ability to capture bandpass-filtered images of chemiluminescence in a methane flame.

This work presents a novel method of actively-cooling an image sensor for embedded imaging of extreme temperature flows using a dielectric cooling liquid, using existing technologies to expanding the capabilities of optical diagnostics. This thesis discusses the challenges associated with actively-cooling a small-scale image sensor in high-temperature environments while maintaining a small package size. Large amounts of heat generated by extreme environments must be directed away from the image sensor to prevent damage to electronic hardware. System reliability and safety challenges are discussed for thermal management of a small form-factor system.

Chapter 2

Background

The push for advancements in high-speed flight capabilities has resulted in increasingly complex computational models that require high resolution to provide accurate prediction data. Experimental testing of high-speed systems is crucial in the evaluation of prototype designs, helping to validate computational models as well as differentiate between true flow structures and mathematical artifacts in simulations.

High-speed aerodynamic testing can be difficult due to current technological limitations both in flight experiments and wind tunnel testing, especially concerning hypersonic regimes. Hypersonic flight vehicles often are unrecoverable and have slow data downlink speeds due to bandwidth limitations. This results in high-cost experiments that are difficult to image and have minimal onboard measurement sensors.

In order to gain an understanding of the applications of high-speed flow measurement techniques, it is beneficial to discuss high-speed wind tunnel configurations and the challenges associated with data collection in those environments. High-speed ground test facilities provide more measurement capabilities than flight experiments that have space and weight restrictions, allowing individual sections of test articles to be isolated for performance evaluation without bias from other components. Tests can mimic specific flow conditions to study phenomena such as turbulent boundary layer transition, aerothermal loading, shock-propagation in supersonic inlets, and unstart flow characteristics of scramjet engines.

2.1 Scramjet Airbreathing Propulsion

Supersonic combustion ramjets (Scramjets) are a class of ramjet engines designed for operation at speeds above Mach 6. They operate by compressing the incoming air and

injecting fuel at supersonic speeds. Figure 2.1 breaks down the stages of a generic airframe-integrated scramjet engine.

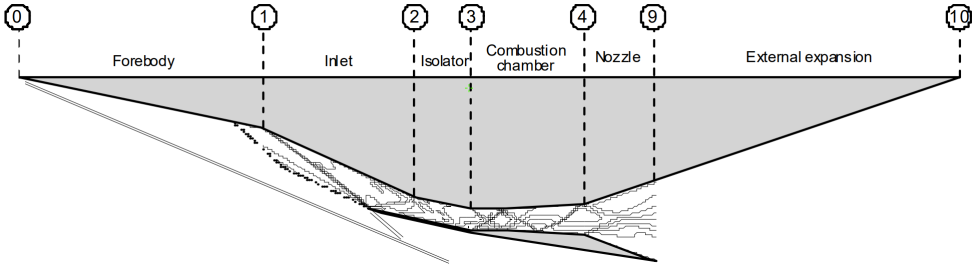

Figure 2.1: Scramjet engine flow stations [1]

Air is compressed via a system of shock waves, replacing mechanical compressor components seen in gas-turbine engines with supersonic aerodynamic compression. Unlike traditional ramjets, scramjets only partially compress and slow the high-speed air, avoiding energy losses produced by a normal shock wave system [35]. The isolator contains a shock train that further compresses the air and separates the inlet from adverse pressure effects created by combustion in the combustion chamber. Because the compression chamber in a scramjet has a fixed geometry, the pressure at the combustion chamber entrance can vary depending on the flow conditions. Scramjet flow paths are generally airframe-integrated, so the entire aft portion of the aircraft acts as part of the engine nozzle [36].

Scramjet designs have been widely studied due to the complex internal aerodynamics, influencing the design of most hypersonic test facilities. Compression and slowing of hypersonic flows to speeds less than Mach 5 within the airbreathing system allows use of pre-existing supersonic wind tunnel facilities to simulate the flow through individual stages of the scramjet engine without requiring hypersonic inflow conditions. Scramjet aerodynamics are still not well understood, with issues arising at off-design operation such as engine unstart and combustion instability that restrict scramjet designs to specific operating conditions.

2.2 Supersonic Test Facilities

Simulation of supersonic flight conditions in test facilities requires large amounts of driving power. This makes it difficult to produce continuous flow for large test sections, especially at hypersonic speeds. At speeds above Mach 5, stagnation temperatures can impact the material structure of wind tunnel, limiting many tunnel designs to short-duration run times on the order of seconds as portrayed in Figure 2.2.

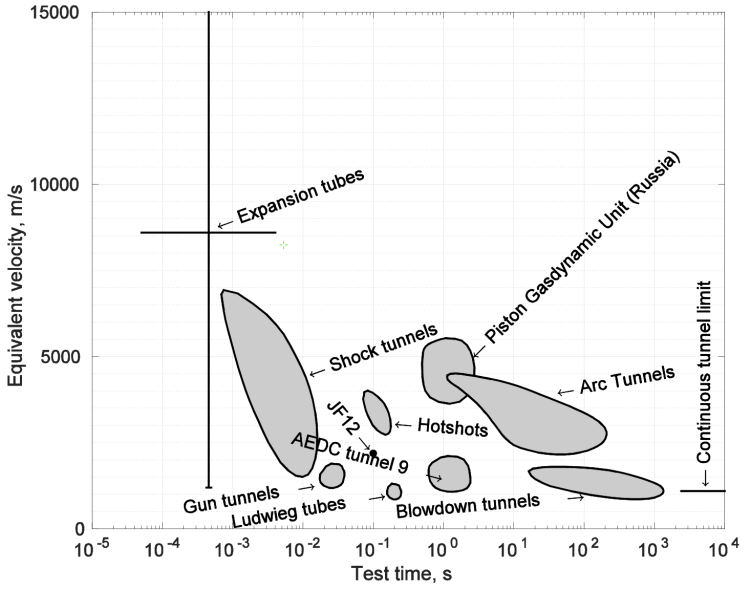

Figure 2.2: Facility run durations and velocity ranges assuming air as the test gas [2]

2.2.1 Continuous-Flow and Blowdown Facilities

Continuous-flow wind tunnels are advantageous for test campaigns where numerous flow condition and test article configurations are desired. These tunnels allow test configuration modification during a tunnel run without needing to restart experiments for each desired condition. Continuous flow tunnels have pressure and enthalpy limitations, lacking the required flow energy to produce these conditions.

The Arnold Engineering Development Complex (AEDC) Von Karman Facility houses three continuous flow supersonic tunnels, Tunnel A, B, and C. Tunnel A can operate from

Mach 1.5 to 5.75, while Tunnels B and C can produce hypersonic flows at Mach 6, 8, and 10. These facilities each have a test article injection system that can be used to remove a test article from the flow for modification while the tunnel is still operating [2, 37].

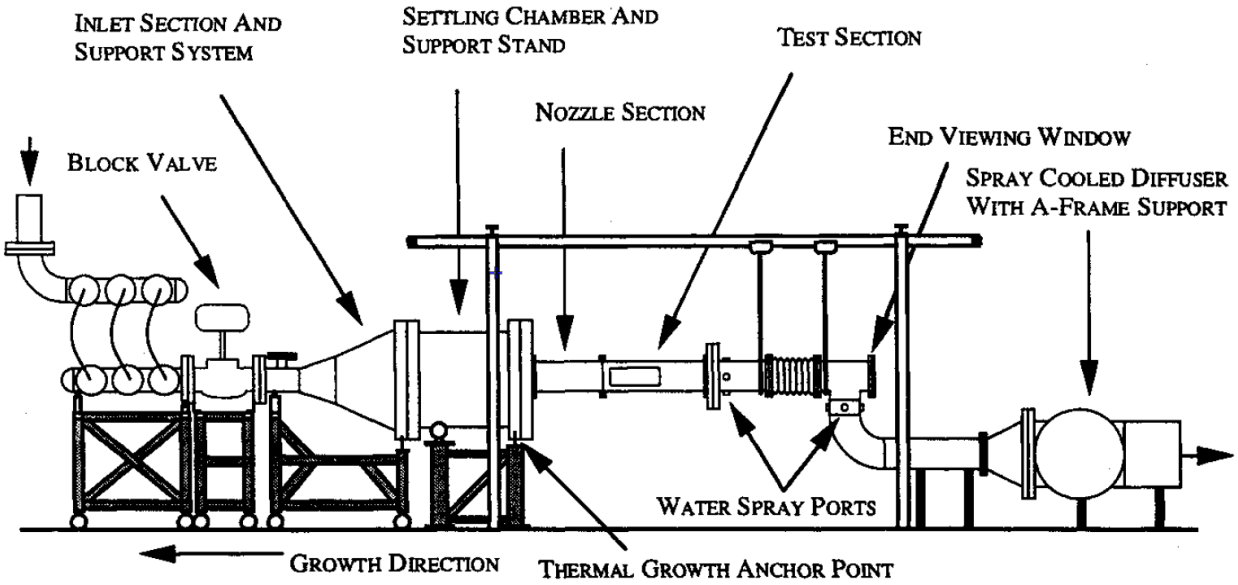

Figure 2.3: Supersonic Research Facility (RC-19) schematic [3]

The Supersonic Research Facility, Research Cell 19 (RC-19) at Wright-Patterson Air Force Base, shown in Figure 2.3, is a continuous flow, direct-connect supersonic wind tunnel designed to operate between Mach 1.5 and Mach 5. It can provide continuous flow with mass flow rates up to 30 lbm/s. RC-19 is equipped with three windows around the test section and a fourth window on the downstream end of the diffuser, making it convenient for optical diagnostics of fuel injection, flameholder operation, and shock wave/boundary layer interactions (SBLI) of hypersonic airbreathing propulsion components. It can operate up to 2860 kPa stagnation pressure at 1,300°F [3, 38].

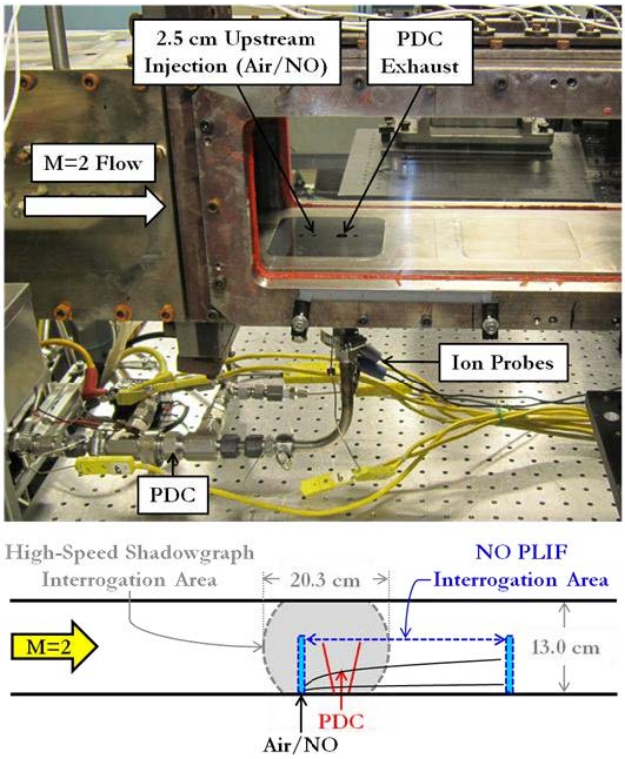

Figure 2.4: Pulsed detonation combustor configuration in RC-19 [4]

Ombrello et al. [4] studied enhanced mixing of a pulsed detonation combustor (PDC) in RC-19 by injecting fuel and oxidiser perpendicular to a Mach 2 flow. The study used high-speed shadowgraphy and NO planar laser-induced fluorescence (PLIF) to observe the PDC plume and shock propagation. Figure 2.4 shows the floor plate injection locations and a schematic of the shadowgraph and NO PLIF interrogation areas. This study revealed that elevated temperature and pressure conditions and large vortex generation are necessary for reliable scramjet combustion.

Blowdown facilities can provide long-duration experiments on the order of seconds to minutes. They operate by heating up a source of air, usually in the form of a high-pressure bottle field, to a desired flow enthalpy and contain a nozzle to accelerate the flow to the flight speed. Blowdown facilities can be assembled in a direct-connect configuration, where a test article is directly attached to the tunnel nozzle. Direct-connect configurations can be used for combustor testing without the need for test article inlets and isolators. Blowdown tunnels

can also support free-jet testing, where a test article is inserted into the high-enthalpy flow. This provides the capability for testing inlet and isolator designs [36, 39]. Blowdown tunnels can raise the enthalpy of air via combustion heating, electric heating, or arc heating.

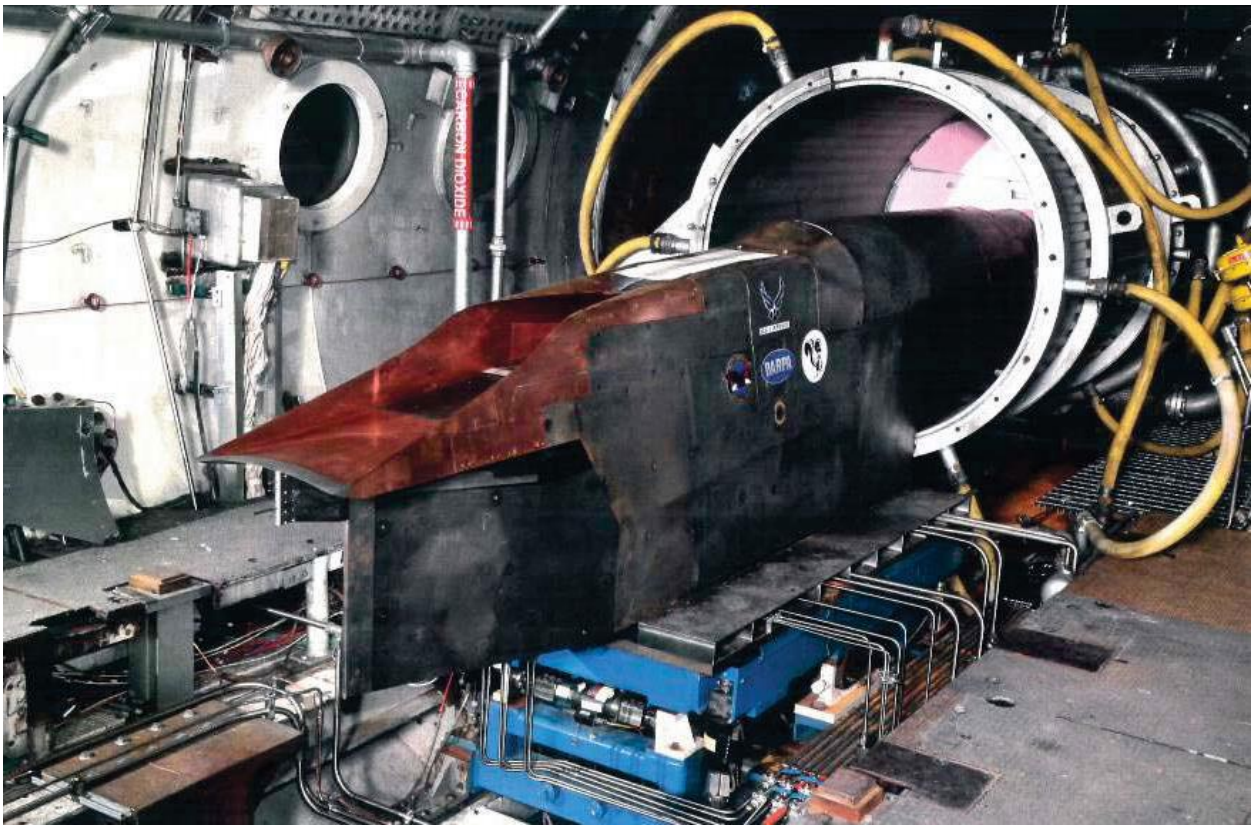

Figure 2.5: DARPA FaCET test article installed in APTU [5]

Combustion heating provides a convenient method of heating the flow, although the air in a combustion-heated tunnel is spoiled by the reaction products of combustion. An example of a combustion-heated blowdown facility is the AEDC Aerodynamic Propulsion and Test Unit (APTU). The APTU can be configured either for direct-connect or free-jet flows at Mach 3.1 to Mach 7.2. APTU was used to support the DARPA FaCET program (Figure 2.5), which aimed to develop a turbine-based combined cycle ram/scramjet engine [5, 40].

Electric heating allows a clean source of air to be heated using external heating elements that do not interact directly with the flow. Existing electric heating elements often have

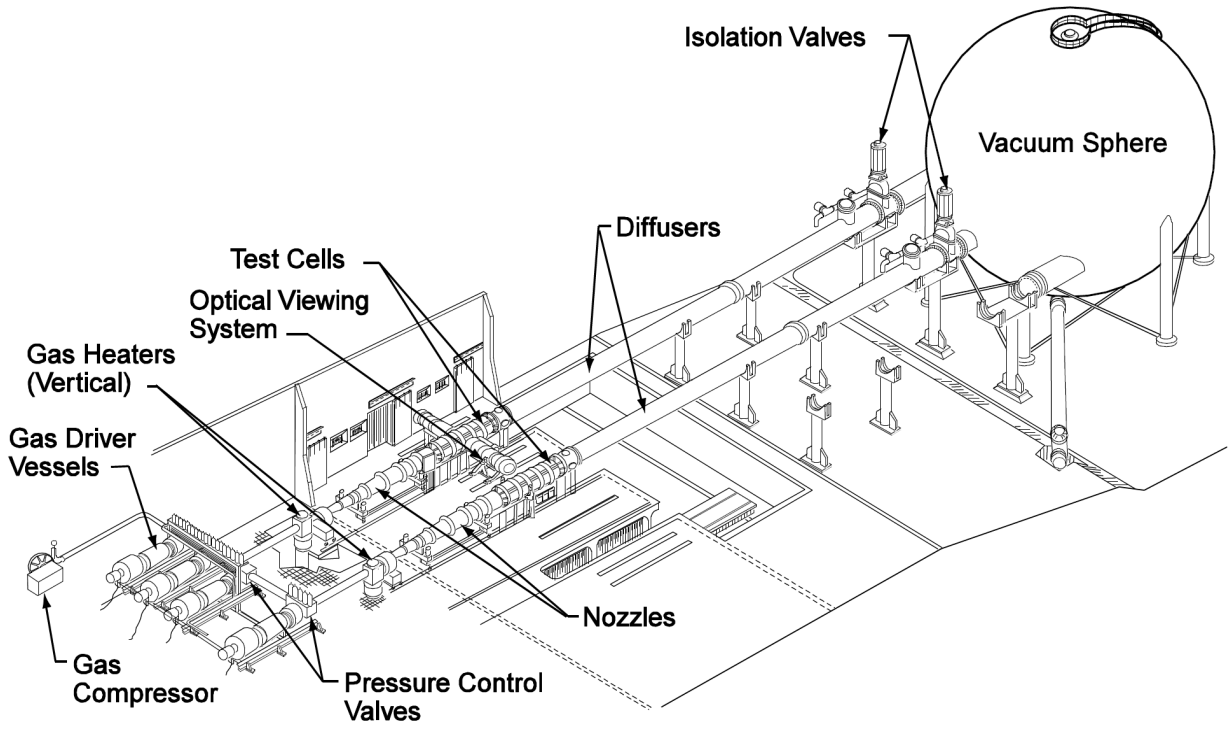

Figure 2.6: Hypervelocity Wind Tunnel 9 schematic [6]

difficulty achieving higher temperatures. The AEDC Hypervelocity Wind Tunnel 9 (Figure 2.6) is an electrically-heated free-jet blowdown tunnel that can operate at Mach 7, 8, 10, 14, and 18 using various nozzles using pure nitrogen as a working fluid [6, 41, 42]. The Tunnel 9 Mach 7 nozzle 9 was used for structural testing of the infrared seeker window of THAAD in 1996 [43].

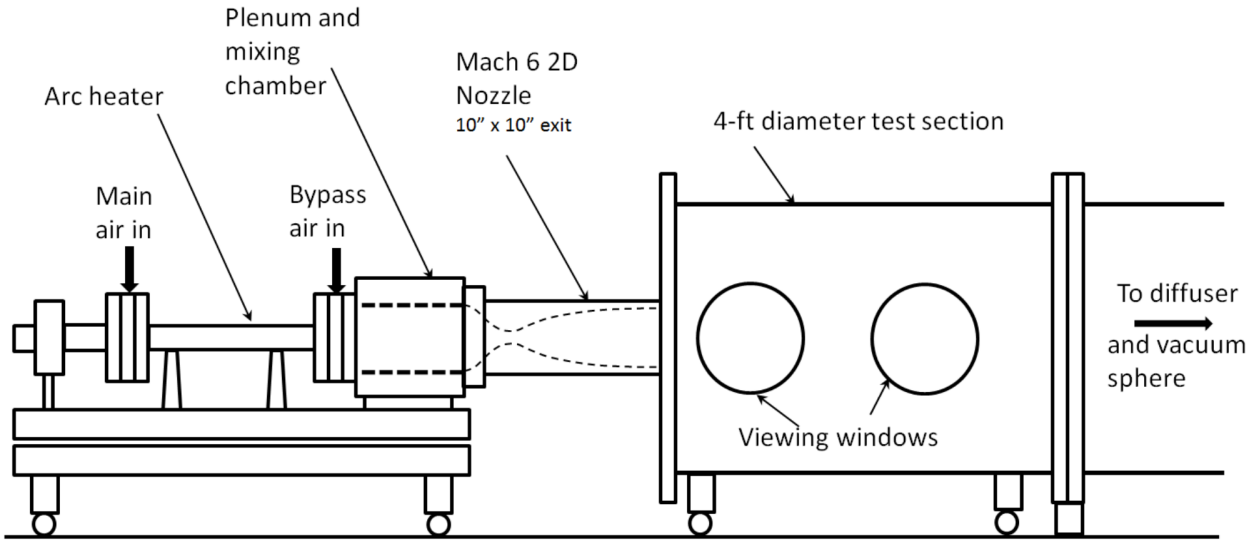

Figure 2.7: AHSTF schematic [7]

Arc-heated facilities can achieve elevated stagnation temperatures, although they require a considerable amount of power to arc electrodes in the stagnation chamber, often on the order of tens of megawatts. Electrode material is often released into the flow, generating species that would not be present during a flight experiment [36]. The NASA Langley Arc-Heated Scramjet Test Facility (AHSTF), shown in Figure 2.7, is an arc-heated blowdown facility that can operate in semi-free jet or a direct-connect configurations with nozzle capabilities between Mach 2.2 and Mach 8.0. The AHSTF has contributions in testing of the NASP and X-43A Hyper-X hydrogen-fueled scramjet engines, as well as the HIFiRE 2 hydrocarbon-fueled scramjet engine [7, 44].

2.2.2 Impulse-Type Facilities

A limitation of continuous-flow and blowdown facilities stems from difficulties generating high-enthalpy hypervelocity flows for extended durations due to high power and resource requirements. A variety of impulse-type tunnels have been developed with the ability to achieve much higher flow velocities by moving a slug of high-velocity air for a very short duration.

Shock tubes provide a basis for most impulse-type tunnels. They consist of a high-pressure driver section and a low-pressure driven section. The driver section consists of a long, high-pressure reservoir, often filled with air or a lightweight gas to produce high Mach flows. Shock tubes are operated using an impulse mechanism, often in the form of a burst-diaphragm or a fast-acting actuator valve. This mechanism separates the driver section from a driven section that is often at atmospheric pressure or evacuated to produce a large pressure differential to drive the gas.

Shock tunnels (Ludwieg tubes) are a variant of shock tubes that replace a simple tube driven section with a driven section that consists of a converging-diverging nozzle, a test section, and a vacuum tank. This allows a shock wave to move through the high-pressure region and the flow to expand through the nozzle to generate flow conditions up to Mach 20. Shock tunnel run times are limited by the size of the high-pressure driver section and the speed of the moving shock, only providing milliseconds of quasi-steady state flow [39, 45].

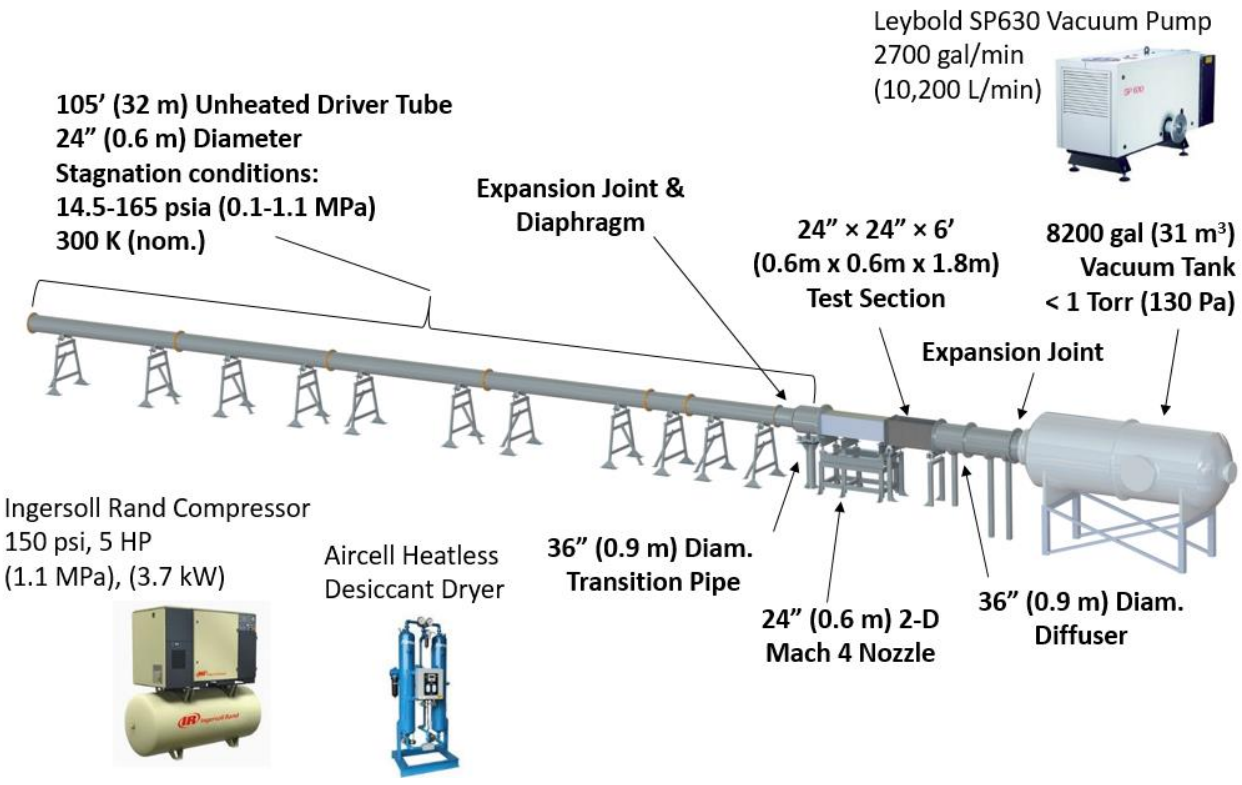

Figure 2.8: UTSI Mach 4 Ludwieg tube schematic [8]

The UTSI TALon facility contains a Mach 4 Ludwieg tube (Figure 2.8) and a Mach 7 Ludwieg tube. These facilities can simulate Reynolds numbers similar to those produced in the AEDC Von Karman Facility tunnels, allowing the Ludwieg tubes to be applied for similar experiments at different run conditions. Both facilities operate using a burst-diaphragm, although future upgrades to the Mach 4 Ludwieg tube plan to implement fast-acting valve operation [8, 46].

Calspan LENS I and LENS II are reflected shock tube facilities that use a double-diaphragm system to reflect shocks that heat and pressurize the driver gas to high enthalpies before expanding through a nozzle into the test section. LENS I/II use hydrogen or helium as the driver gas in order to achieve high Mach numbers. LENS I can simulate Mach 6 to Mach 22 flow conditions, while LENS II can simulate Mach 3 to Mach 7 flow conditions. These facilities have contributed to studies for the NASA Shuttle STS vehicle and the X-43 scramjet engine, the AFRL HIFiRE-1 and HIFiRE-5 tests, and the Boeing HyFly scramjet and the X-51 Waverider testing [47, 48].

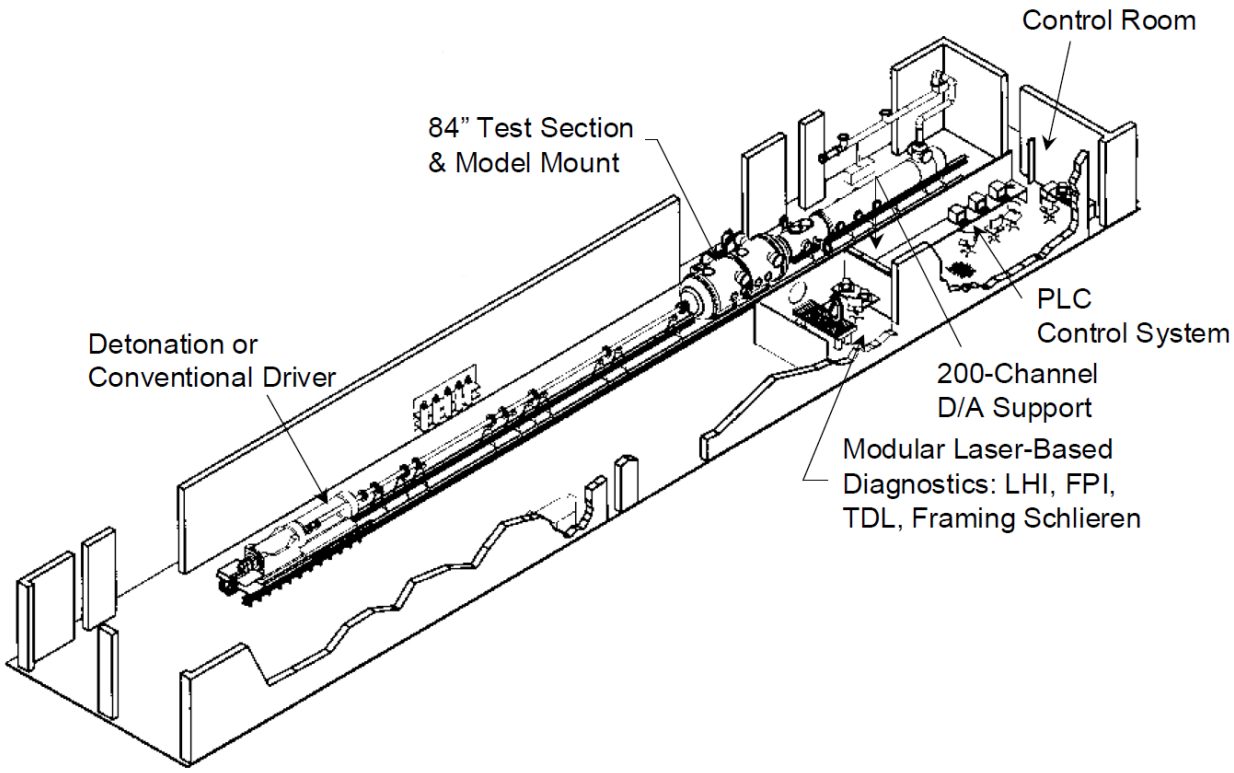

Figure 2.9: HYPULSE schematic [9]

Another type of impulse facility is the expansion tunnel. Expansion tubes operate similarly to shock tubes. Unlike shock tubes, they do not contain a nozzle to accelerate the driver gas, and instead include a secondary tube and diaphragm further downstream in order to further accelerate the primary shock. Expansion tube run times are often limited to less than 1 ms duration, often on the order of hundreds of microseconds. The NASA HYPULSE facility (Figure 2.9) is an expansion tube that can simulate flight conditions from Mach 5 to Mach 25. HYPULSE has contributed testing for the X-34, Mach 10 testing for the Hyper-X program, and testing for the Space Shuttle thermal protection system [9, 36].

2.3 Thermal Management for High-Speed Flow Applications

High-speed flows often generate extreme thermal environments that can be damaging to embedded electronic hardware. This often requires implementation of cooling techniques to remove large amounts of heat for extended duration experiments. Cooling techniques such as passive heat sinks and fan cooling have low heat-exchange capabilities, requiring cool ambient air to be circulated near hardware in order to maximize cooling [49, 50]. High speed test article hardware often requires more extreme liquid or gas cooling, with high-enthalpy environments transferring large amounts of heat directly into the immersed test article.

Alternatively, water cooling can provide thermal management via channels in the walls of a test article or wind tunnel wall. This often requires complex coolant routing that can lead to extensive fabrication time and high-cost components. Water cooling is often used for high temperature ground test environments that require tunnel wall and hardware cooling because of the availability of a continuous supply of fresh water [51]. This presents a limitation for flight applications that require cooling with the added consideration of weight-saving for high-speed flight tests.

Dielectric liquids are non-conductive cooling liquids that prevent electronic discharges to electronic hardware, making them ideal for applications where a cooling liquid may need direct contact with electronics. This removes thermal resistances associated with indirect cooling systems. Immersion cooling is often used to provide thermal management to data centers and provide an insulator for high-voltage electronics, reducing energy consumption from heat generation [52, 53]. Immersion cooling with a closed-loop system constantly replenishes fresh coolant into the hot environment. Some dielectric fluids have low viscosities, allowing coolant to flow through confined regions of complex coolant paths. For high-temperature flow environments, dielectric coolants provide an advantage because they have the potential to regulate heat generated both by a harsh thermal environment as well as directly from measurement hardware. Dielectric cooling liquids can have thermal conductivity values that

are a fraction that of water and that can be similar to the thermal conductivity of air, allowing these liquids to act as a thermal insulator between sensitive hardware and extreme environments.

Jimenez et al. [54] used the dielectric coolant Fluorinert FC-72 to validate thermal management of an immersion-cooled system with narrow channel flow. The system was intended to be implemented in aircraft with high heat flux. The study found that two-phase immersion cooling provided heat dissipation an order of magnitude higher than existing systems. Although the mentioned studies utilize two-phase immersion cooling to improve thermal management, the system presented in this work proposes a single-phase immersion cooling solution to enable imaging directly through a liquid-phase coolant, avoiding optical distortions from phase change to a gaseous state.

Liquid cooling using a closed-loop flow path can be evaluated by measurement of the rate of heat transfer from a thermal environment to the flowing coolant. Equation 2.1 relates heat transfer rate based on a mass flow rate.

$$\dot{q} = \dot{m} c_p \Delta T \tag{2.1}$$

Analysis of the heat transfer rate can help determine capabilities of closed loop cooling systems for various flow rate and thermal conditions.

2.4 High-Speed Instrumentation for High-Enthalpy Flows

2.4.1 Conventional Probe Sensors

Conventional measurement techniques often consist of instrumenting probes that are limited to point-measurements. This requires an array of sensors in order to acquire spatial information. Flush-mounted pressure transducers can gather pressure information near a wind tunnel or test article wall. It can be difficult to infer information about complex flow fields simply from wall conditions. Pressure rakes can be used to gather an array of data

points in a flow, although this intrudes the flow and can change the flow phenomena occurring in the region of interest. Temperature measurements can be gathered using thermocouples and hot-wire anemometry, although these instruments also intrude the flow. Intrusive probes can present issues especially when simulating high-speed flow environments at flight conditions where an incoming laminar flow is desired to minimize unnecessary thermal loading on a test article or flight vehicle model. Point measurements of pressure and temperature can be used to estimate additional properties such as flow velocity using simplified forms of the Navier-Stokes equation, although these measurements may be improved by obtaining full flow field information using optical techniques.

2.4.2 Optical Measurement

Non-intrusive optical diagnostics provide a convenient platform to measure spatial flow phenomena without disrupting the flow under observation. This allows measurement of flow properties including velocity, Mach number, pressure, temperature, density, and even species composition in reacting flows. This information can be used to reconstruct 2D sections of a flow field or in some cases entire 3D regions of a flow to predict transient and long-term temporal implications of design geometries. Optical measurement techniques have a vast and widely expanding range of applications including observation of coherent flow-structure interactions in high-speed flows [11, 22, 55, 56], attitude detection in seeker heads using infrared (IR) image sensors [57], and combustion analysis in reacting flows [27].

Scientific camera systems have the ability to provide extremely high temporal and spatial resolution images. This enables a variety of optical measurements to be employed for characterization of flows, including particle image velocimetry, digital-image correlation for stereoscopic viewing, pressure- and temperature-sensitive paint applications (PSP/TSP), surface oil flow visualization (OFV), and chemiluminescence imaging. Figure 2.10 shows a circular scramjet model that was modified to gain optical access for observation of shock propagation during startup and unstart characteristics in choked flow conditions.

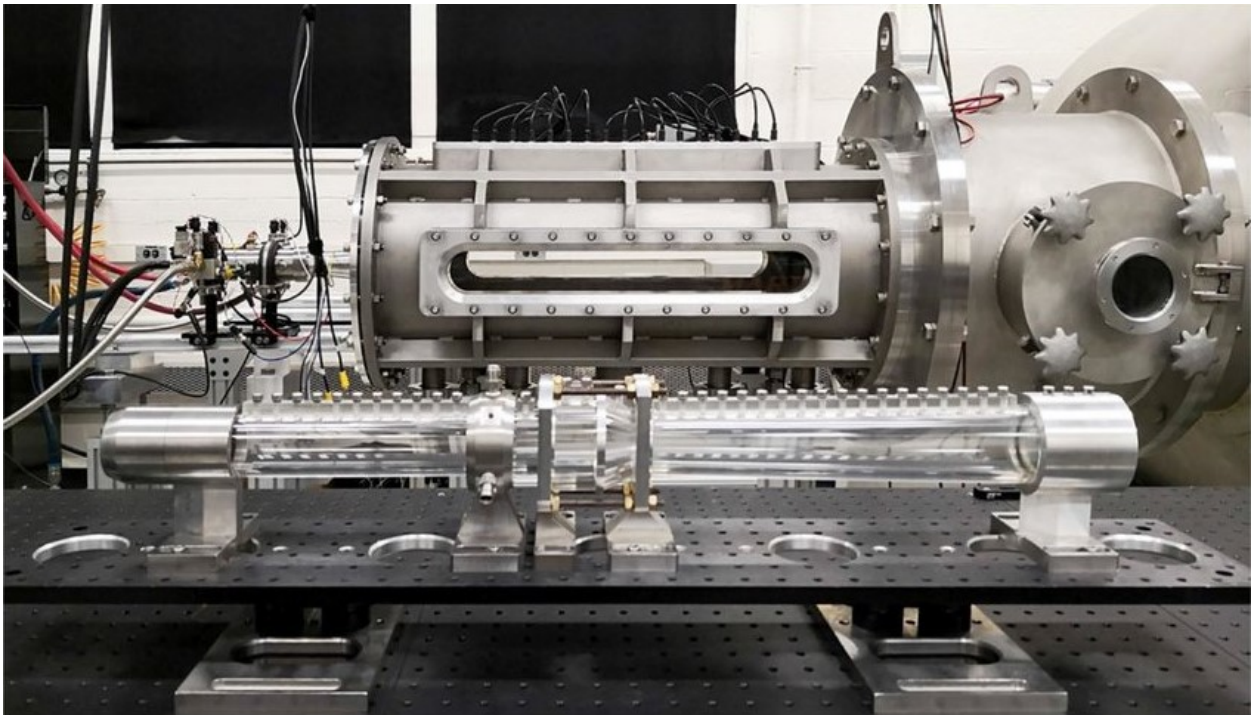

Figure 2.10: Transparent circular scramjet model in the ACT-II arc-heated hypersonic wind tunnel facility [10]

Systems that use traditional scientific cameras can be expensive with a large footprint, often requiring either a system of mirrors and magnifying optics or extensive modification to test articles in order to gain optical access to confined flows. For flight experiments, on-board sensor equipment is often kept at a minimum for weight-reduction purposes. External imaging is not realistic for flight tests due to the high rates of travel and difficulties tracking high-speed vehicles.

Optical diagnostics of combustion environments can provide information about reacting flows. Many high-speed reacting flows are not-as-well understood, causing there to be large interest in development of optical systems for observation of high-speed combustion phenomena.

Optical fibers have been implemented in some cases with a borescope design to monitor combustion chambers by utilizing flame luminosity to determine thermal effects on the inside of the chamber [28, 58]. These designs enable the use of larger camera systems with higher data collection rates that can exist outside of the low-access region of interest, although

the fiber optic bundle packets affect the image with wasted space around each individual fiber, producing "dots" instead of pixels. This limits the application of this type of system to inspection and monitoring of combustion environments without a continuous image to be able to identify flow structures and correlate motion of particles in a region. Borescope cameras are also generally limited to lower image resolutions due to physical space requirements of individual fibers. These constraints make optical fiber systems inconvenient for high-speed flow measurement where a high-resolution image may be necessary in order to track particle motion to observe flow structures.

Periscopic imaging systems have also been developed to view afterburner plumes to gather information about shock formation and flame propagation [59–61]. Periscopes use a series of mirrors to redirect light toward the imaging system either using a fiber bundle for transmission to an external camera or by installing an embedded camera into the scope bore. Periscopic systems have been used to locate flame front and exhaust locations by digitally combining images from multiple probes for stereoscopic viewing [59]. Because these probes are designed to extend near the centerline of the flame, additional shock fronts are generated over the probe head, which can alter the downstream plume [60]. This can be detrimental to internal flow paths where additional shock generation can increase back pressure and result in unstart of a model by choking the flow.

With the rapid development of image sensor technology, board-mounted CMOS image sensors have become readily available at a fraction of the cost of traditional scientific cameras used for optical diagnostics. Although these sensors sacrifice some resolution in relation to traditional large-scale systems, their small form factor presents the possibility for them to be embedded directly into test articles and flight vehicles to observe regions that have historically been difficult to measure without significant test article modifications. Small board-mounted CMOS image sensors have only been implemented for a handful of aerospace research applications, presenting opportunities to perform novel measurements for

airbreathing propulsion systems. Eagan et al. [11] embedded a miniaturized imaging system into a subscale scramjet model with a Busemann streamline-traced inlet (Figure 2.11).

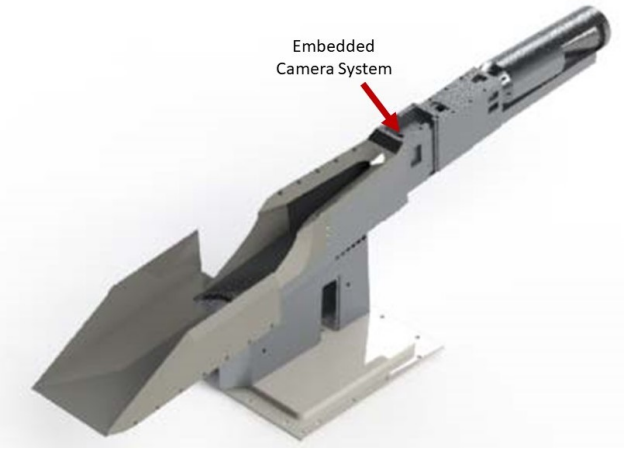

Figure 2.11: Busemann inlet-isolator scramjet model (raceway covers removed) [11]

This inlet-isolator model is capable of back pressure and discrete angle-of-attack adjustments to simulate different flight conditions. The miniature imaging system was embedded on the cowl-side of the inlet-isolator transition region to perform ultraviolet OFV and PSP measurements of the SBLI of the cowl shock with the body-side isolator duct region. This work aided in the identification of major flow features including the shock impingement and reflection locations as well as identification of the recirculation region. Figure 2.12 displays a single frame of the oil-flow visualization of the SBLI inside the scramjet model, showing the recirculation region downstream of the reflected oblique shock.

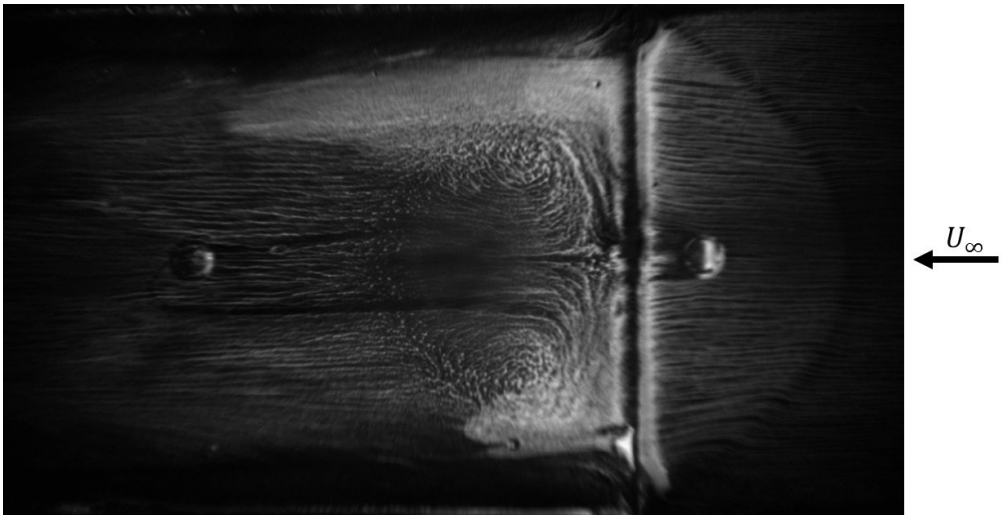

Figure 2.12: OFV Showing SBLI in Buseman inlet-isolator system [11]

Another study performed by Pandey et al. [12] at Sandia National Laboratories embedded two miniature cameras into a conical test article (Figure 2.13) to observe fluid-thermal-structure interactions (FTSI) of a thin panel on a wedge in hypersonic flow.

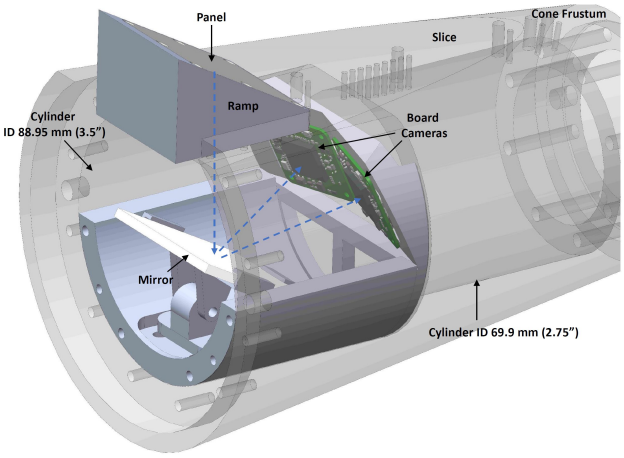

Figure 2.13: Internal-DIC schematic inside conical test article [12]

This study observed a speckle-patterned thin panel on a wedge using a two-camera configuration to determine out-of-plane displacement and panel deformation using digital image correlation (DIC). This type of study is useful for evaluation of aerothermal deformation on hypersonic vehicles that utilize thin-walled airframe components for weight-saving.

2.5 Chemiluminescence Imaging

Chemiluminescence is the process by which photons are emitted from a chemical reaction causing excited molecules to shift down to the ground state, producing light at measurable wavelengths that allow identification of reaction regions. This phenomena occurs during combustion processes, making it a particular interest for a variety of aerospace propulsion applications, including hypersonic propulsion detonation imaging [62], shock front visualization of a rotating detonating combustor [29], and flame stoichiometry imaging [30]. By filtering the light emitted from combustion flames using optical bandpass filters, information can be gathered by imaging at various wavelength bands to understand flame structure as well as regional reaction features. The formation of excited species can be represented in a general sense by Equation 2.2.

$$A + B \rightarrow C^* + \text{other radicals} \tag{2.2}$$

Here, A and B represent the combustion reactions. C^* represents the chemiluminescence radical being measured. The light radiation of the excited radicals shifting back to the ground state can be represented by Equation 2.3.

$$C^* \rightarrow C + hv \tag{2.3}$$

Here, C represents the ground-state product species. The energy contributed to photon emission is estimated using Planck's equation, where h is Plank's constant and v is the emitted frequency in a black body.

Chemiluminescence imaging in combustion applications focuses on locating and quantifying partial decomposition products of the reaction. Chemical reactions near the flame front generate large amounts of local heat, resulting in light emission from excited species. For hydrocarbon flames, the narrow band wavelength radicals, methylidyne (CH^*), Diatomic

carbon Swan Band emission (C_2^*), and OH^* can be observed to characterize the state of the flame [29–31]. CH^* and C_2^* partial reaction product formation in flames emit light at wavelength bands centered at 427nm and 513nm, respectively. OH* emission is centered around 310nm wavelength, although this is outside the visible spectrum and requires an intensified camera in order to capture sufficient light to collect images [27].

Background emissions produced by soot and other radicals can emit light at similar wavelengths to CH^* and C_2^* chemiluminescence, especially broadband emissions produced by CO_2^*. This makes it necessary to filter out background emissions to locate and measure CH^* and C_2^* radical formation. Additional bandpass filters offset from the desired wavelength can be used to subtract background emissions and isolate CH^* and C_2^* chemiluminescence using a four-line image processing method [25, 33, 34].

When characterizing airbreathing combustors, localized equivalence ratios can be measured in stabilized turbulent premixed flames. The intensity ratio of C_2^*/CH^* can be used to determine regional as well as overall-flame equivalence ratios [32]. Equivalence ratio measurements aide in the measurement and understanding of heat release, pollutant generation, and flame stabilization properties [30].

Optical diagnostics have traditionally been a primary method of observing high-speed, high-temperature flows due to their non-intrusive ability to obtain spatial information about a region of interest. Diagnostics of internal high-enthalpy flows traditionally require test article modifications in order to gain optical access for large-scale camera equipment. By embedding small board-mounted image sensors directly near a flow, novel flow measurements can be taken for flow regions that are not well understood without requiring extensive test article alterations. With the implementation of immersion cooling, high-temperature environments may be imaged in order to better understand chemical reactions and flow structures within combustion environments.

Chapter 3

Actively-Cooled Miniature Imaging System Design

This work aims to develop an actively-cooled miniature imaging system (ACMIS) such that it can view low-access, high-speed flows that often produce harsh, high-temperature environments for sensor hardware. A cooled image sensor housing (CISH) was designed to provide active cooling directly to the image sensor and lens assembly. The internal geometry of the CISH was designed to flow dielectric coolant through and around the lens assembly to regulate the thermal environment around the entire sensor package. A back end closed-loop cooling system (CLCS) continuously replenishes coolant to the CISH and maintain optimal sensor temperatures.

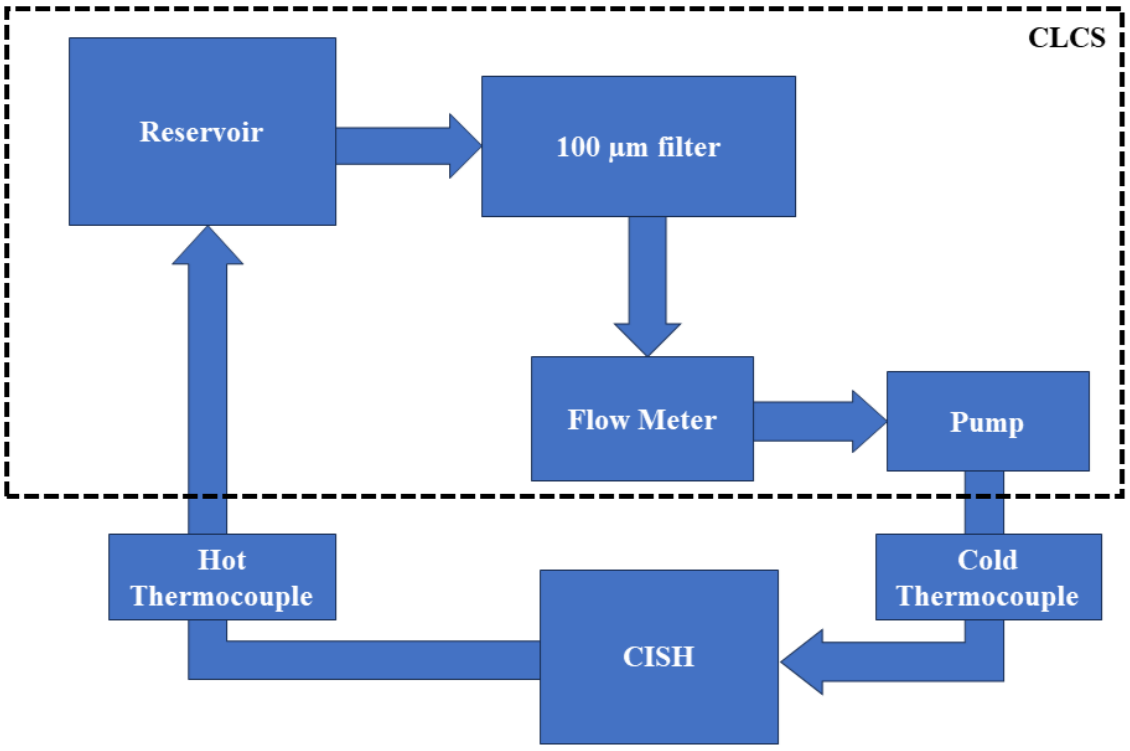

Figure 3.1: ACMIS block diagram

This system was optimized for deployment into the Supersonic Research Facility (RC-19) at Wright-Patterson Air Force Base. Bench-top thermal experiments were conducted in order to replicate the conditions that would be experienced by the system in the RC-19 combustor. Chemiluminescence experiments were performed to evaluate the system's ability to capture flame decomposition products using selected bandpass filters. The thermal exposure threshold for ACMIS was targeted to 1,300°F based on stagnation temperatures expected at the RC-19 tunnel wall [3, 38]. This provides a convenient temperature threshold to push the limits of single-phase cooling using a dielectric fluid. During a combustion cycle in RC-19, the facility pre-heats the air around 800°F over an extended duration during the tunnel idle. Combustion periods that expose the tunnel wall to 1,300°F typically last 20-30 seconds depending on experimental conditions and necessities. The tunnel hardware that ACMIS is designed for operates at 31 psia, providing little concern for system reliability based on pressure conditions.

3.1 Component Breakdown

3.1.1 Imaging System

The imaging system presented in this work is an extension of the system developed in Eagan et al. [11, 22]. A Sony IMX273 image sensor was selected for this work based on previous successful integration with the data processing hardware from experiments detailed in Eagan et al. [11]. This sensor is a monochromatic, global shutter, CMOS image sensor capable of delivering 1.58 MP resolution (1456×1088 pixels) at 225 frames per second (fps) for 10-bit ADC, and can be sub-sampled to achieve even higher frame rates. The IMX273 has an optical format of 1/2.9, allowing the use of standardized M12 format lenses. A Vision Components MIPI camera module (Figure 3.2) was selected for this system to interface the image sensor with a back end data collection and processing system (DCPS) to transmit images to a workstation for post-processing.

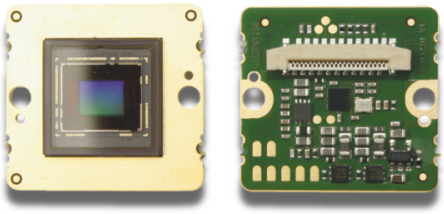

Figure 3.2: Vision Components MIPI camera module with Sony IMX273LLR sensor [13]

A benefit of using M12 lens format is the wide availability of COTS lenses that can be integrated or replaced depending on the intended application. An Arducam M12 low distortion camera lens was selected for this work. This lens provides a 93° FoV along the diagonal for a 1/2.9" sensor format, and has a working wavelength range between 400 nm and 700 nm, making it ideal for visible spectra imaging analyses. The low-cost of these lenses provides convenient interchangeability in the event of lens damage or multi-lens experiments.

Due to high light intensities produced during combustion, optical filters are implemented to filter desired light bands to provide better detail and prevent image sensor saturation. In order to perform chemiluminescence imaging, optical filters centered at 430nm and 520nm were directly adhered to two separate lenses to observe light emission from radicals consistent with other studies that observe CH^* and C_2^* emissions. This is intended to determine the ability of ACMIS to capture images similar to traditional systems while flowing dielectric coolant directly around the image sensor and lens.

Figure 3.3 depicts the 430nm optical filters assembled with the camera module. The optical filters were adhered to each lens using Norland Optical Adhesive NOA 61, a UV-cured adhesive that is optically-transparent with exceptional bonding properties between metal and glass. These lenses were mounted to separate M12 mounts, so that they could be calibrated in advance of experiments to provide a consistent working distance when interchanging lens assemblies.

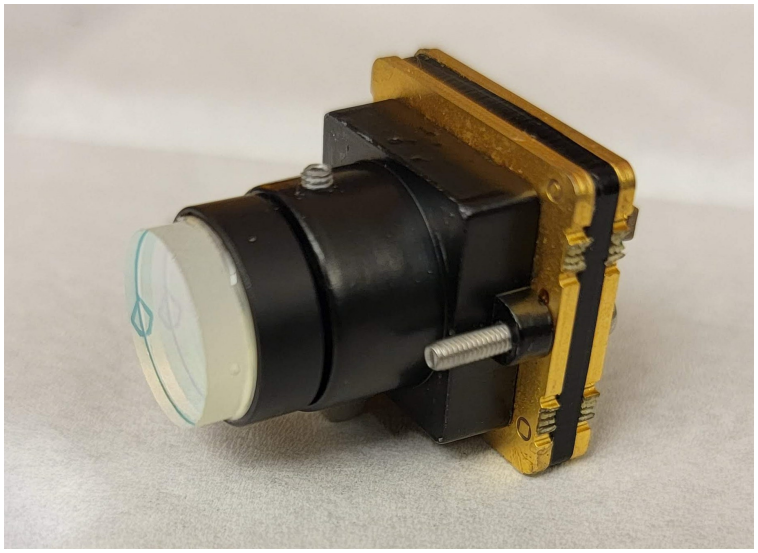

Figure 3.3: Camera module assembly with 430nm optical filter adhered directly to lens

The CISH was designed to protect the camera module by regulating its thermal environment through active cooling, while still maintaining convenient assembly for component swap-out based on the need for multiple optical filters. Considering the extreme thermal environment the CISH is designed to be exposed to, much of the housing assembly needed to be adapted by replacing traditional materials with high-temperature compatible components. The majority of the machined CISH components were manufactured using 316L stainless steel due to the high temperature corrosion resistance of 316L stainless steel.

The CISH is designed with a 1.4 inch by 2.2 inch footprint to have the capability of being embedded into a 2.5 inch wide elliptical shoulder-seal insert to replace similar window components. The front barrel of the CISH has a 1-inch diameter meant to extend 0.5 inch depth for a modified tunnel insert. The CISH is designed around a tunnel insert that would have a 0.1 inch thick shoulder to compress the window with a 0.5 inch thru-hole for the viewing region. This geometric constraint provides a 50° field-of-view with the CISH installed into a model. The lenses used with this analysis were focused to an effective working distance of 2.6 inches that would reflect the mid-plane of the tunnel cross-section, giving an approximate 3-inch field of view in the streamwise direction along the tunnel mid-plane.

Graphite gaskets infused with a stainless steel mesh are used to create seals between the stainless steel components as well as to provide a seal around the protective fused silica window. These gaskets replace traditional gasket material in order to withstand high temperature compression. Two gaskets compress the viewing window between the front insert/adapter and the front portion of the CISH. These provide a seal to prevent hot gasses in the tunnel from entering the housing or escaping out of the tunnel as well as provide a seal for the coolant to flow around the front of the camera lens. The assembly, depicted in Figure 3.4, consists of a melting furnace adapter, front housing, housing cover, and an aluminum back plate.

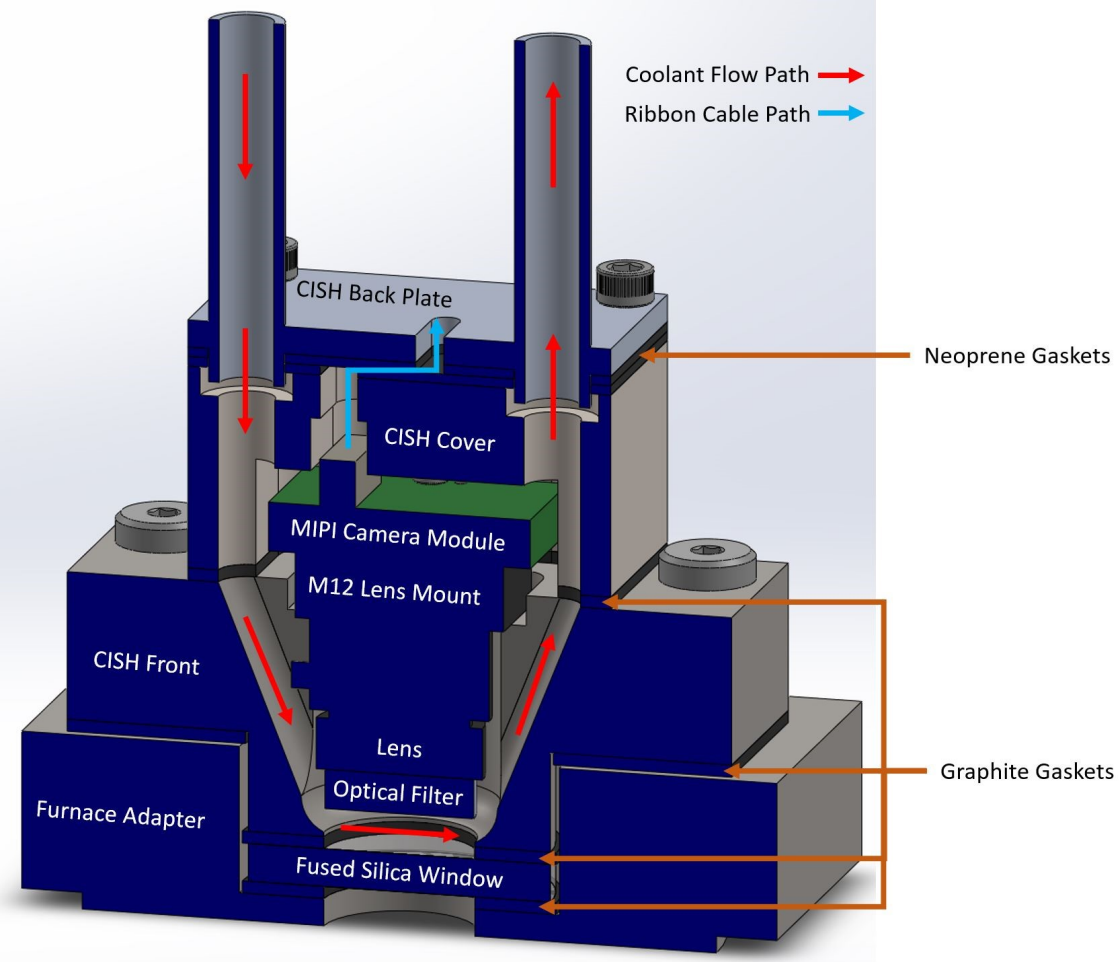

Figure 3.4: Cross-section of CISH assembly with camera module and optical filter installed

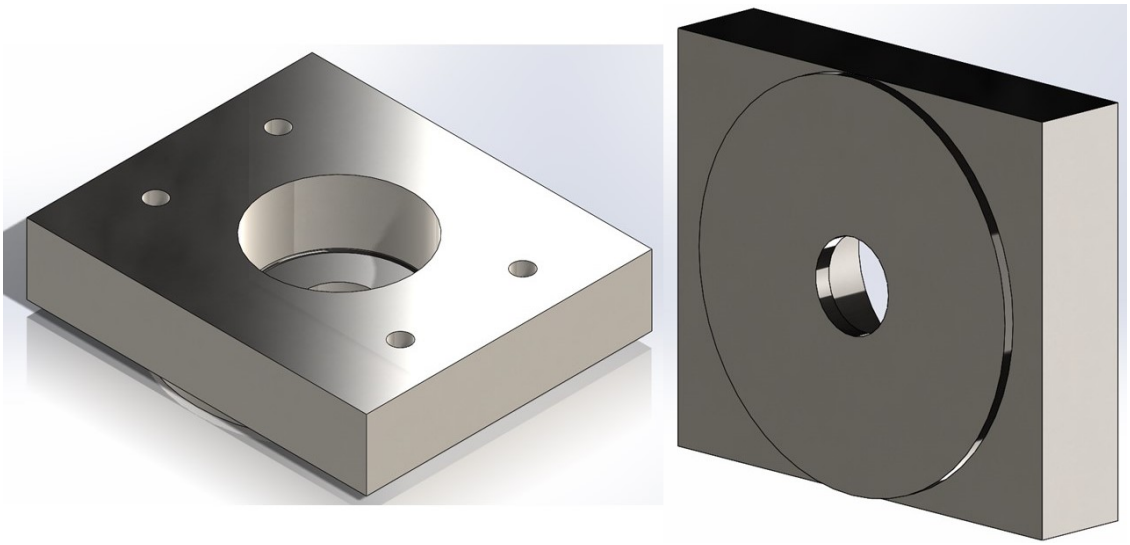

Figure 3.5: Melting furnace adapter

The melting furnace adapter (Figure 3.5) is designed to replicate the geometry from an elliptical wind tunnel wall insert that this system would be embedded into. It was designed to mate to a melting furnace detailed in Section 4.2. The front of the furnace adapter includes a circular shelf to center the adapter with the melting furnace. Four #10-24 threaded holes secure the CISH housing to the furnace adapter with a counterbored hole to provide a compression surface for the window gaskets.

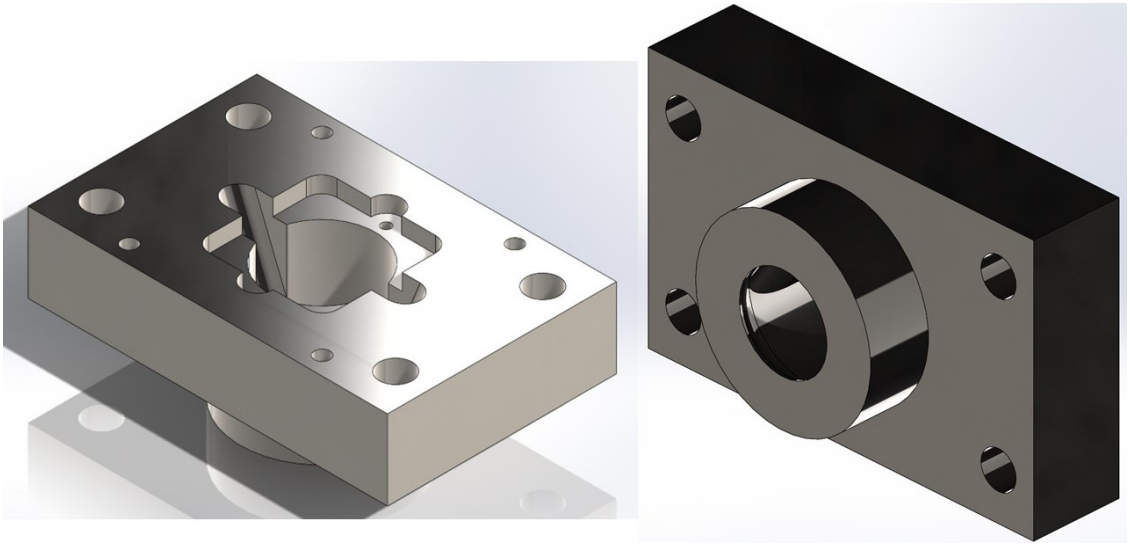

Figure 3.6: Front housing

The CISH front housing (Figure 3.6) provides compression around the fused silica window and graphite gasket assembly, while providing a mounting surface for the camera module and a flow path to direct the coolant around the front of the lens and optical filter. It has four thru holes for mating to the furnace adapter. The front housing includes four #4-48 threaded holes to secure the housing cover to the front housing. Two #1-72 threaded holes secure the camera module directly to the front housing. Two ramps direct the coolant to the front of the housing to improve flow around the front of the lens assembly.

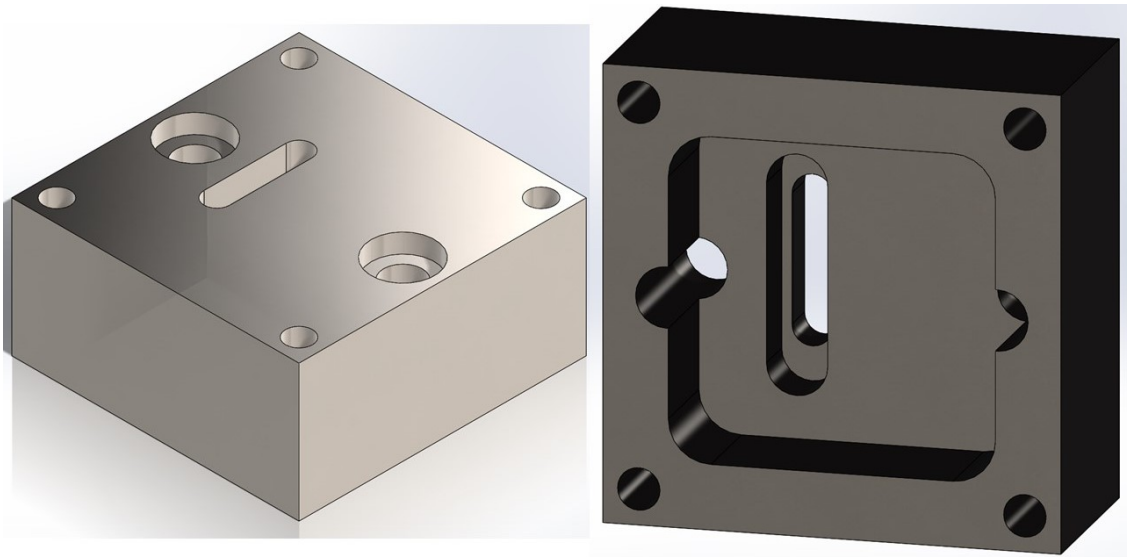

Figure 3.7: Housing cover

The housing cover (Figure 3.7) provides a sealed enclosure to direct the coolant toward the front of the module, while fully immersing the module in the dielectric coolant. Four thru holes mate the housing cover to the front housing. Two counterbored holes provide a flow path to direct the flow toward the ramps on the front housing. A slotted thru hole provides a pass through for the camera module ribbon cable while minimizing any stagnation regions behind the PCB.

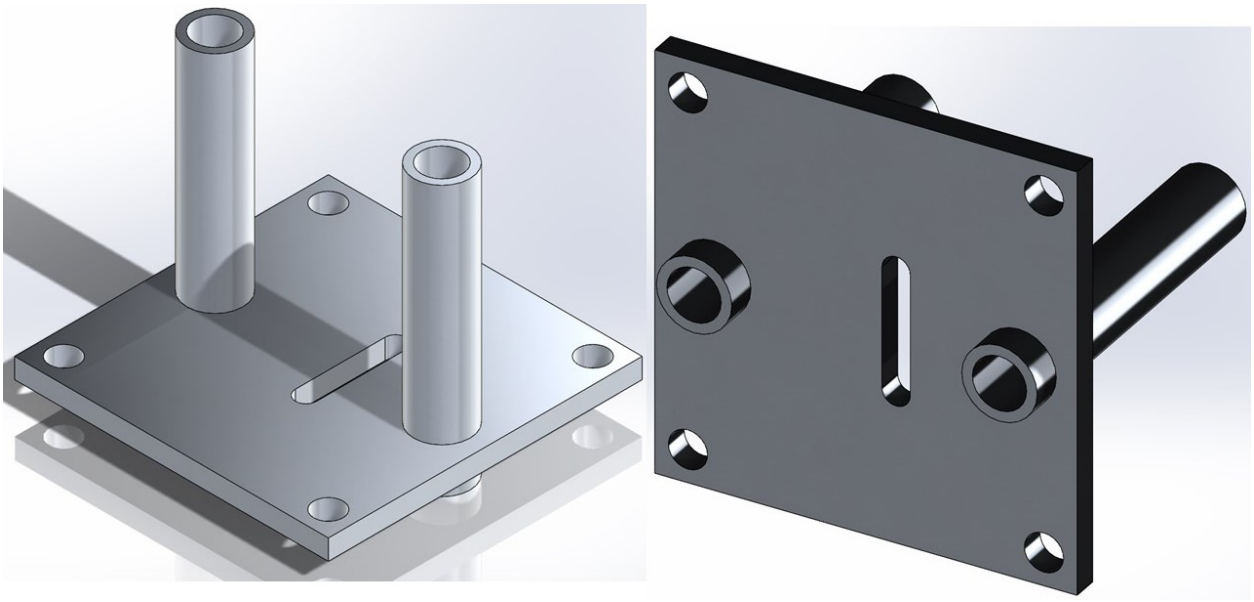

Figure 3.8: Housing back plate

The CISH back plate (Figure 3.8) provides compression for two neoprene gaskets (shown in Figure 3.4) that seal between the housing cover and the back plate to provide a sealed routing for a ribbon cable to pass through. The back plate has two machined tubes protruding from the back face in order to mate the cooling path to standard compression fittings.

T-joint compression fittings are assembled to each of these tubes (shown in Figure 4.6) to instrument Type J thermocouples (McMaster #39095K95) on the incoming cold and outgoing hot coolant paths to characterize heat removed from the CISH by the coolant. Type J thermocouples are capable of operating up to 825°F. These thermocouples have grounded probes that provide a 0.3 second response time with a ±0.18°F (±0.1°C) measurement resolution. Thermocouple data was processed by a General Tools 4-channel thermocouple thermometer and offloaded via a RS-232 protocol port to the remote workstation.

3.1.2 Data Collection and Processing System

The backend data collection and processing system (DCPS) described in this work is an adapted version of the system detailed in Eagan et al. [11]. Figure 3.9 breaks down the DCPS into its major components. The DCPS primarily consists of COTS components, although experimental constraints required custom printed circuit boards (PCBs) to be manufactured to account for long transmission distances. The DCPS is programmed and operated using a MATLAB GUI on a remote workstation.

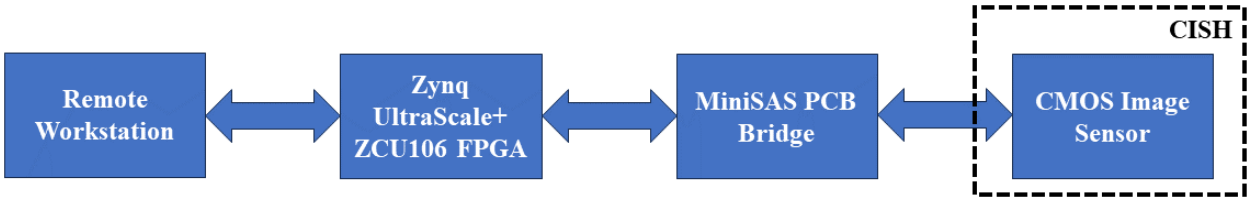

Figure 3.9: DCPS block diagram

The IMX273 image sensor transmits image data using a 4-lane MIPI protocol at a 1.5 Gb/s transmission rate across a standard 22-pin FPC ribbon cable. MIPI protocol limits the transmission to approximately 1 ft transmission length. In order to provide an adaptable system such that the image sensor does not need to be directly near other system hardware, a re-timing and redriving PCB was implemented to extend other hardware away from the harsh thermal environment. In order to prevent signal degradation, a custom PCB was manufactured to transmit the data using a miniSAS twin-axial cable to the FPGA. MiniSAS cables are capable of high-speed data transmission even when creased within confined spaces, making them a convenient platform for confined test article routing.

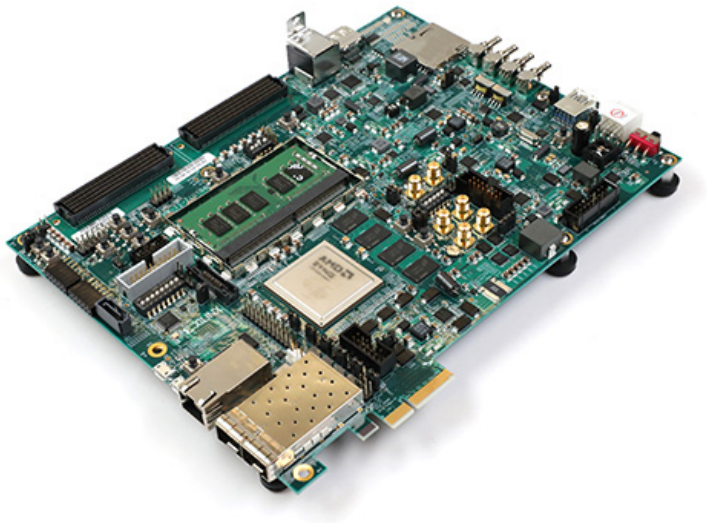

Figure 3.10: Zynq Ultrascale+ MPSoC FPGA [14]

A Zynq Ultrascale+ MPSoC FPGA was used to provide power, data processing, storage, and camera configuration and triggering. This FPGA was mounted onto the Xilinx ZCU106 evaluation board (Figure 3.10) equipped with a custom mezzanine card. A remote workstation, connected to the evaluation board via ethernet, was used to program the FPGA in MATLAB and to store offloaded data. The assembled FPGA system is capable of receiving 40 Gb/s of image data from up to 4 image sensors over MIPI interface, allowing for future expansion of this system for multi-camera module configurations.

3.1.3 Closed-Loop Cooling System

The coolant selected for use with the ACMIS is 3M Fluorinert Electronic Liquid FC-72 [63]. This coolant is chemically and thermally stable, designed to operate either for single or two phase cooling applications with a boiling point of 133°F. Because this coolant is routed in front of the image sensor, it is necessary to replenish the coolant within the housing at a high enough rate to prevent two phase operation. FC-72 also has a kinematic viscosity much lower than water, allowing the coolant to more easily flow through narrow channels with complex routing. FC-72 has an index of refraction of 1.25, unlike that of air [63]. Because

the CISH is designed to flow coolant directly around and through the lens assembly, it was necessary to focus lenses while submerged in the FC-72 coolant.

Under extreme heat conditions greater than 200°C (392°F), flourine-based coolants, including FC-72 which is a perfluorocarbon (PFE), can produce toxic decomposition products including hydrogen fluoride and perfluoroisobutylene (PFIB) [64]. In order to prevent these toxic decomposition products from forming, the closed loop is designed to be able to replenish coolant at a rate high enough to maintain safe coolant temperatures. Future development of this system for long-term and industry use would implement a bypass loop to flush and redirect the coolant in the event of primary pump failure or if the temperature reaches and maintains above a safe threshold.

The closed-loop cooling system (CLCS), depicted by the dashed box in the schematic from Figure 3.1 (also pictured in Figure 4.8), connects to the CISH using EVIL ENERGY nylon braided CPE fuel line hoses with flared aluminum fittings. These tubes are wear- and crush-resistant, allowing them to be deployed for a variety of wind tunnel applications. It is convenient to employ engine fuel-line components for this application due to their pressure and temperature resistances. A 1L EVIL ENERGY overflow/coolant radiator tank provided a reservoir to act as a thermal mass for coolant to dissipate heat into before recirculating into the cooling loop. The reservoir is equipped with a pressure release valve to prevent pressure buildup in the CLCS. The reservoir feeds into an EVIL ENERGY 100 µm inline fuel filter to maintain coolant quality and prevent contamination from recirculated graphite flakes from the gasket material or other system contaminants. An inline flow meter provided flow rates to monitor coolant flow for heat exchange analysis as well as monitoring the flow rate as the pump reaches a steady state flow at high coolant temperatures. A 12V EVIL ENERGY external inline fuel pump was used to drive the flow of coolant. Power was provided to the pump using an external power supply so that the flow rate could be manually adjusted to a desired set value by providing a lower voltage to the pump. The pump was configured to provide fuel at a flow rate of 8 LPM.

Chapter 4

Experimental Analysis and Characterization of ACMIS

Image sensors are sensitive to extreme temperatures. At elevated conditions, the signal-to-noise ratio (SNR) can increase dramatically for temperatures outside the operating range advertised for a sensor. The IMX273 used in this work was thermally-cycled to determine a maximum temperature at which the SNR exceeds an acceptable limit. Figure 4.1 shows 20-image averages of an unilluminated scene to determine standard deviation of the image intensity at various exposure temperatures. These averaged images were scaled between the minimum and maximum pixel intensity values in order to exaggerate the noise near the corners and edges of the sensor generated by heating the sensor.

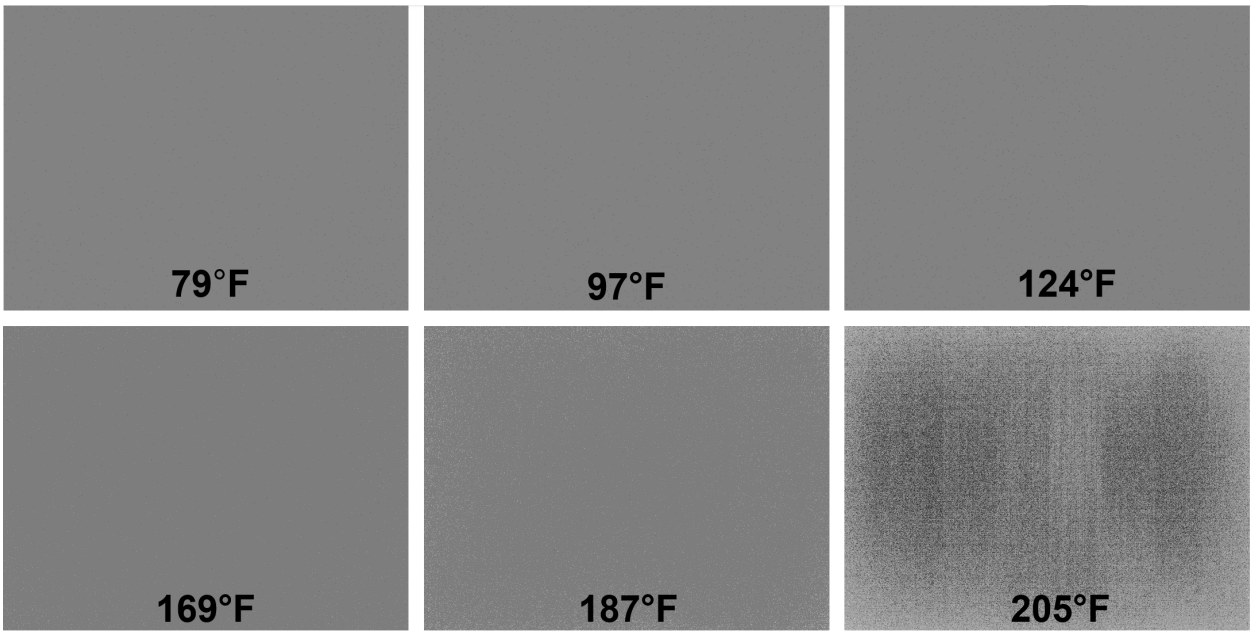

Figure 4.1: Scaled averaged image intensities at intermediate exposure temperatures

Figure 4.2 portrays this effect by visualizing the growth of the standard deviation across averaged series of 20 images at each exposure temperature. An inflection point occurs around 80°C (176°F), where the image noise begins to exponentially increase due to corner heating effects no longer producing a homogeneous SNR. This temperature was selected to design a system that minimizes heating effects in the captured images.

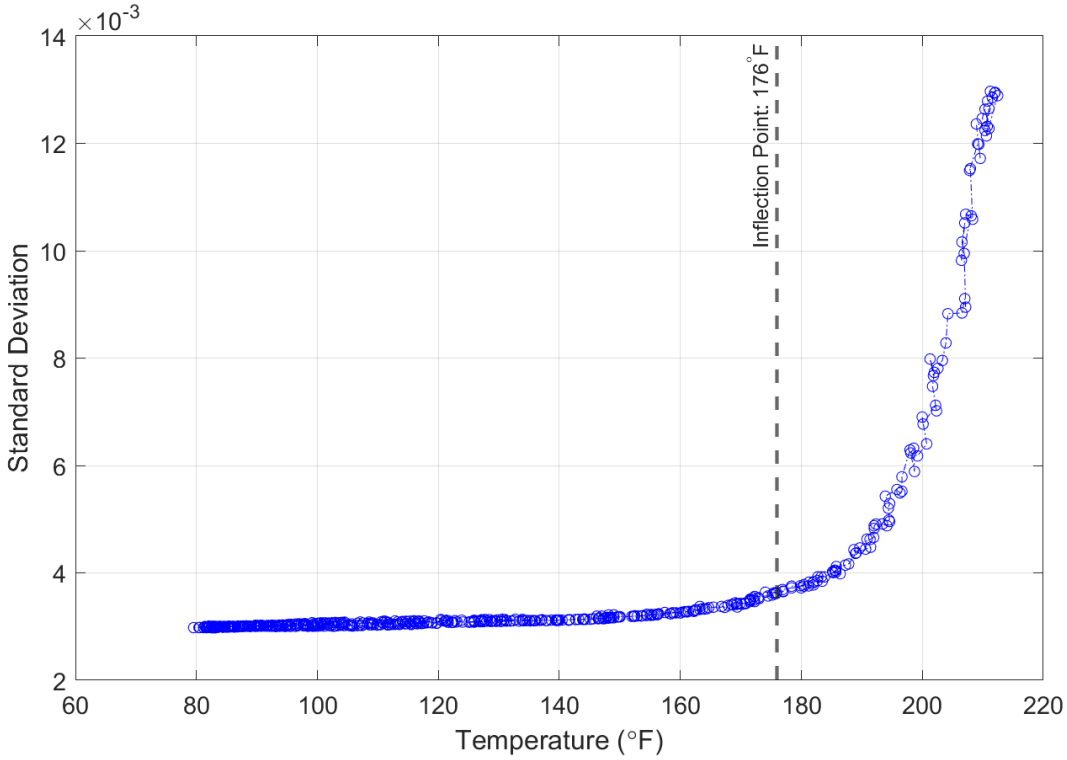

Figure 4.2: Unilluminated image standard deviation as a function of temperature

The active-cooling implementation of the ACMIS was evaluated in phases both due to safety concerns and facility limitations associated with extreme thermal testing. A prototype of the ACMIS was evaluated using a thermal environment chamber to simulate intermediate temperatures. Next the design was iterated to improve the cooling capabilities of the system and mitigate coolant stagnation regions inside the CISH. Further experiments were conducted in the thermal environment chamber to evaluate the updated CISH flow path as well as the improved CLCS. Coolant temperatures were evaluated against chamber set-points to monitor the thermal environment around the camera module at various environmental

temperatures. A final thermal cycling experiment was performed to evaluate the system up to the intended design temperature threshold. The evaluation of the ACMIS was concluded by performing a chemiluminescence imaging to verify the system's capabilities to collect illuminated flame data while coolant was flowing over and through the lens assembly.

4.1 Preliminary Thermal Cycling

Initial investigations into an ACMIS design adapted the housing from Eagan et al. [11, 22] to implement a sealed, closed-loop enclosure to flow coolant directly around the image sensor. This prototype, shown in Figure 4.3, provided a flow path to flow coolant directly around the image sensor and lens package to help manage heat from the outside environment, as well as from the image sensor board. The protective window in this configuration was secured using Norland Electronic Adhesive NEA 155, which has excellent adhesion between glass and metal. This adhesive is heat-cured and has an intermittent service temperature up to 300°C (572°F), which provides sufficient bonding with the reduced thermal exposure provided the heat removal from the coolant.

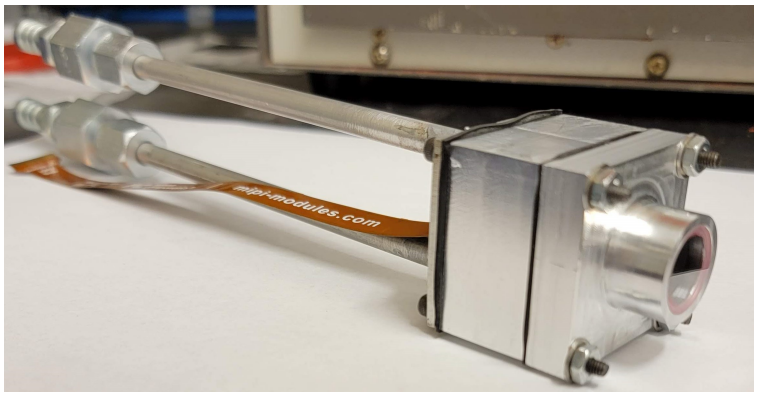

Figure 4.3: CISH prototype configuration

Preliminary experiments were performed in a Delta Design 9023 Environmental Test Chamber. This chamber allows an internal environment to be ramped to a selected set-point from ambient conditions up to 600°F. A custom adapter plate was manufactured to allow the housing to be embedded directly into the wall of the chamber door. The initial configuration

for the thermal cycling prototype (Figure 4.4) consisted of a 1L EVIL ENERGY expansion tank connected to a 5-speed 12V aquarium pump that fed coolant through the housing.

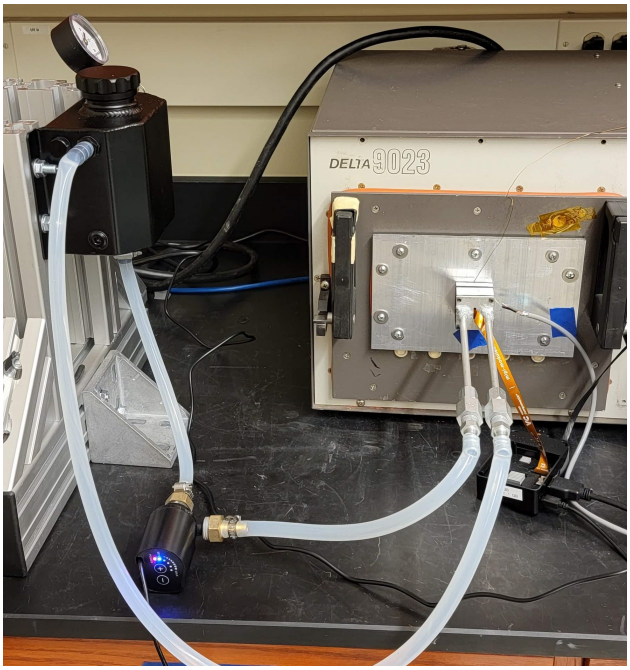

Figure 4.4: CLCS and CISH prototypes configured with Delta Design 9023 Environmental Test Chamber

This pump was used in preliminary thermal experiments to provide an inexpensive platform to evaluate the cooling system performance. Because this pump was designed for use with water, an in-line flow meter was implemented to verify coolant flow rates when using the FC-72 coolant in the closed-loop system with additional resistances on the pump by the piping system. Coolant temperature data and data from thermal conditions near the protective window were gathered using small thermal diodes connected to a LakeShore 218 temperature monitor. One thermal diode was inserted directly near the image sensor inside the CISH to regulate outgoing coolant temperatures. The other diode was mounted on the inside of the test chamber directly near the CISH protective window. Due to the fact that the operation of the DCPS had previously been verified in the work described in Eagan et al. [11] and the viewing region inside the environmental test chamber was unilluminated,

images from the image sensor were collected using a RaspberryPi in order to detect SNR changes as the thermal environment increased.

The ACMIS design was iterated by implementing improvements to the CLCS in order to improve heat removal around the camera module assembly and provide better structural and thermal resistance for the backend CLCS components. Barbed fittings with silicone rubber tubing were replaced with more robust nylon braided CPE fuel lines with flared fittings. An upgraded pump provided better control of flow rates and the addition of an inline fuel filter minimized contaminant circulation throughout the closed loop system. Thermocouples were added to the incoming and outgoing coolant lines near the housing to better characterize the heat transfer to the coolant. Additional experiments were conducted in the environmental test chamber (Figure 4.5) in order to recharacterize cooling properties of the system with the improved CLCS.

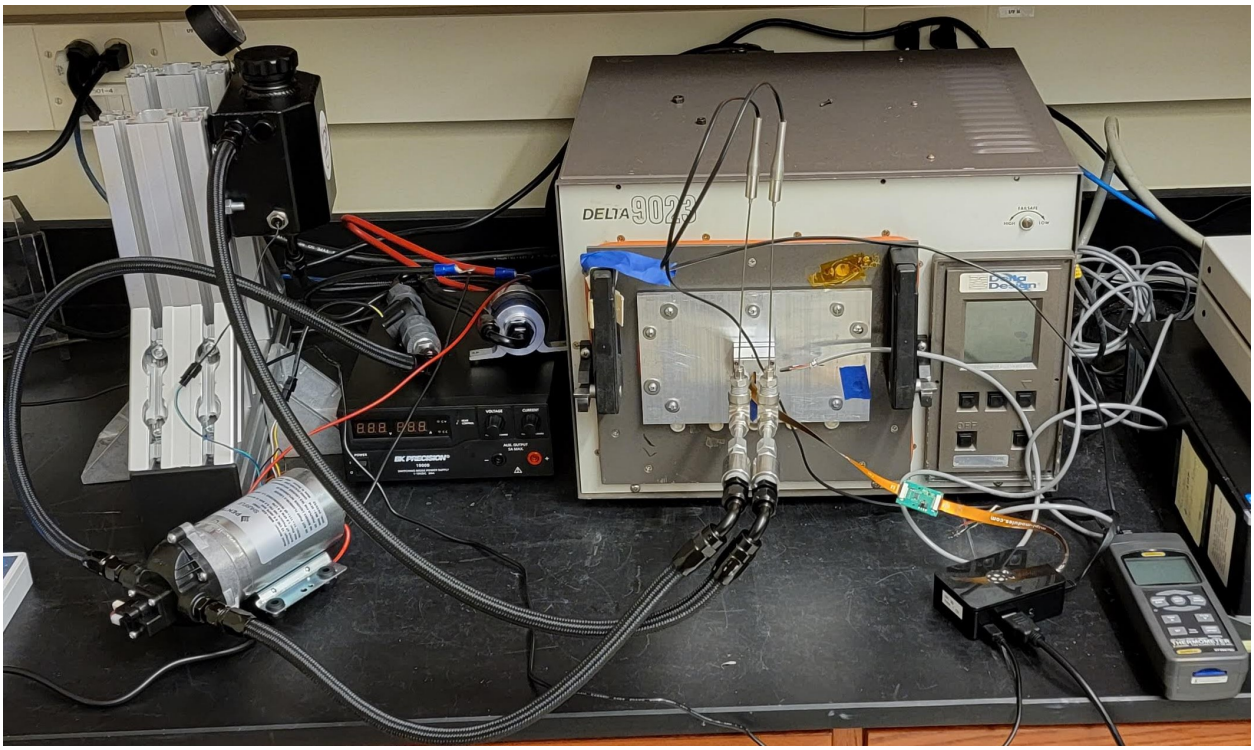

Figure 4.5: Improved CLCS implemented with environmental test chamber assembly

4.2 Extreme Thermal Cycling

An additional system validation was conducted to characterize image quality and thermal management performance up to the target temperature range for the intended application near 1,300°F. This experiment was conducted using an Electric Melting Furnace MF-1000. This furnace is primarily intended for melting metals up to 2,100°F, and is thus designed to cycle to temperatures above the set-point then ramp down to the set temperature, cycling in this manner.

The prototype system from preliminary thermal tests was further modified to withstand much higher temperatures. Figure 4.6 depicts the updated CISH configuration.

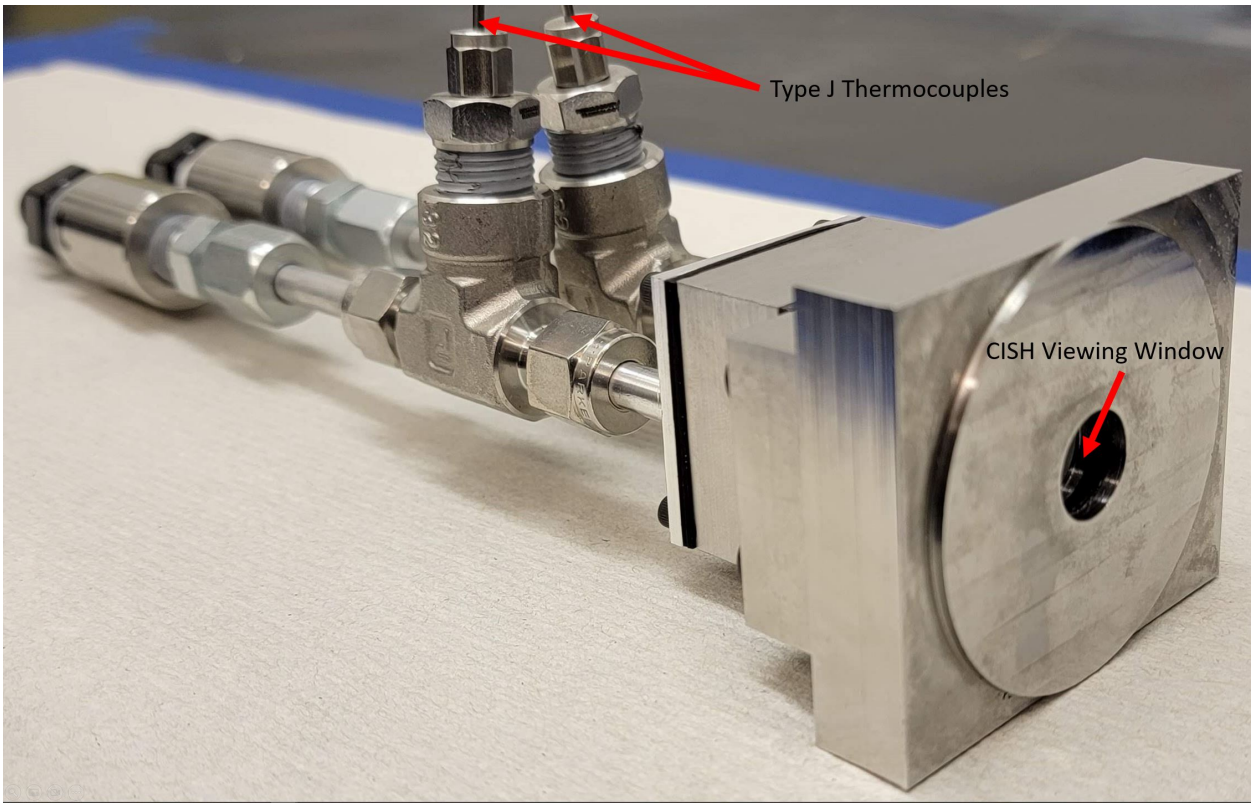

Figure 4.6: CISH melting furnace configuration

Aluminum housing components were replaced with stainless steel, and the internal flow path inside of the housing was optimized to prevent stagnation regions and provide more

efficient cooling capabilities. Figure 4.7 displays the updates to the internal flow path between the prototype and final CISH designs. Neoprene gaskets were replaced with graphite gaskets infused with a stainless steel mesh, providing rigid seals that can withstand higher temperature environments. An adapter was designed to mate the system directly with the melting furnace while replicating a modified wind tunnel wall section motivated by the intended application. Due to thermal limitations of low-viscosity optical adhesives, the updated configuration of the protective window is secured between two compressed graphite gaskets secured by the furnace adapter and the front housing.

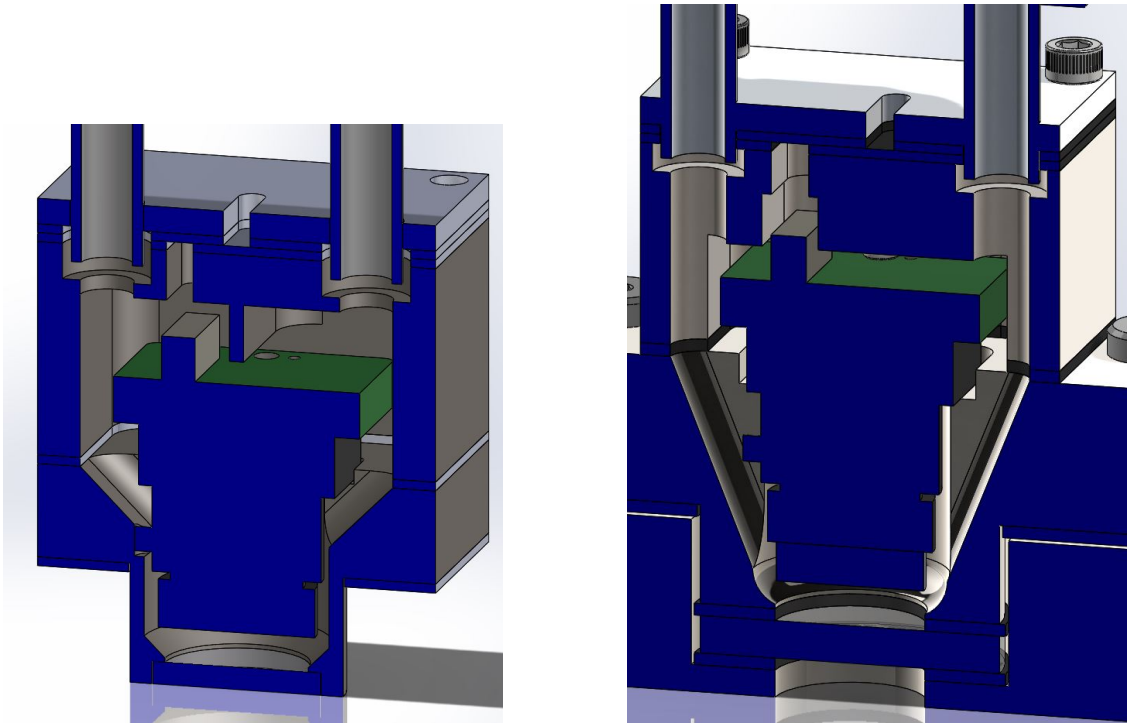

(a) (b)

Figure 4.7: Updates to the Coolant flow path inside the CISH: (a) Prototype CISH flow path, (b) Current CISH flow path

As discussed previously, FC-72 coolant is a flourine-based coolant which can produce toxic byproducts if elevated to conditions above 392°F. In order to safely analyze the performance of the ACMIS at elevated thermal conditions, extreme thermal cycling experiments were performed in a fume hood to avoid personnel exposure in the event of a system failure or major leak. Leak tests were performed independently before heat was introduced from the

melting furnace to ensure proper system seals. The pump was configured to provide 8 LPM of coolant to the CISH. Figure 4.8 depicts the ACMIS installed into the melting furnace.

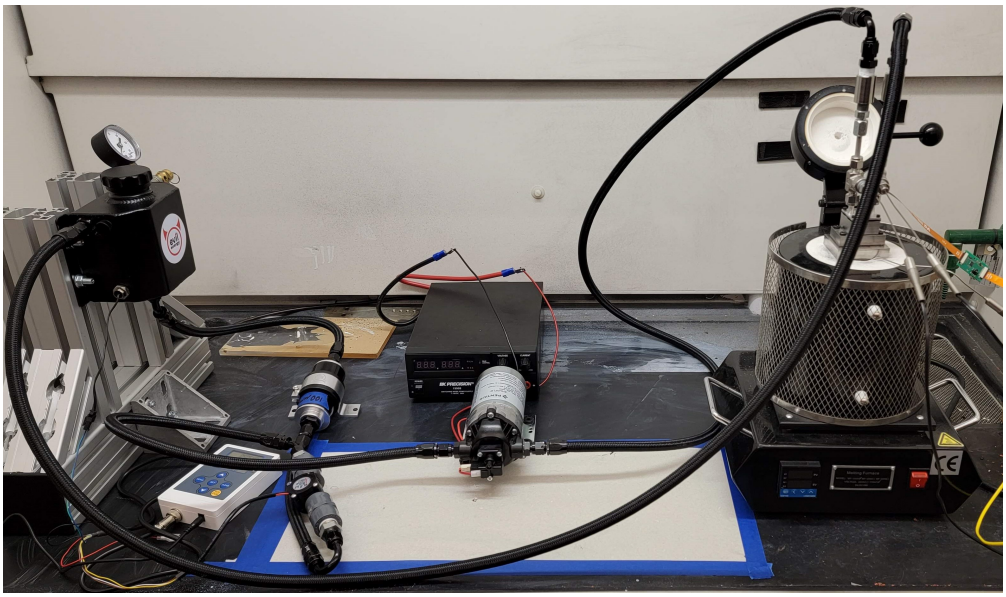

Figure 4.8: ACMIS installed into melting furnace

A Type K thermocouple (McMaster #39095K96) was installed to measure conditions near the protective window due to the furnace thermometer being much lower in the furnace where the heating element is more prominent. This thermocouple is a grounded thermocouple, capable of conditions up to 1,690°F. The K-type thermocouple provides a 0.3 second response time with a ±0.18°F (±0.1°C) measurement resolution. Grounded thermocouples have a measuring probe welded directly to the protective sheathing, providing a fast response time and being susceptible to grounding loops. In order to prevent the Type K thermocouple from grounding to the melting furnace protective cage, insulation tape was wrapped around the probe in locations where the probe would ground to the cage.

4.3 Chemiluminescence Imaging Application

After validation of the thermal capabilities of the ACMIS, an additional experiment was performed to evaluate the imaging system's capability to perform chemiluminescence imaging using integrated bandpass filters. Two bandpass filters are adhered to separate identical

lenses as discussed in Section 3.1. Filters centered at 430 nm and 520 nm were selected to capture spectrally-resolved images of radical light emissions in light bands consistent with studies that isolate CH^* and C_2^* decomposition. Both filters have a full width-half max of 10 nm.

Figure 4.9 depicts the ACMIS configured to perform chemiluminescence imaging by viewing a methane flame produced by a Bunsen burner. Although a Bunsen burner only produces a partially-premixed flame and measurement of equivalence ratio requires premixed flames, this experiment is intended to provide the foundation for future application to fully-premixed flame configurations.

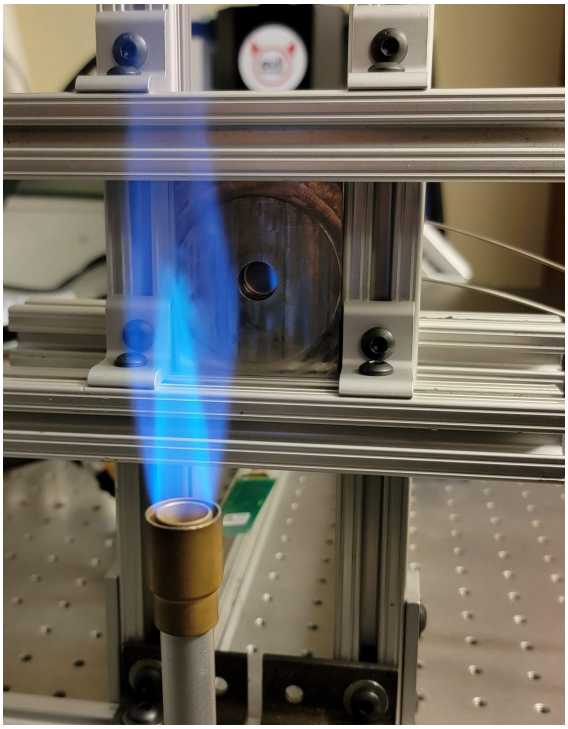

Figure 4.9: ACMIS configured to image methane flame

The Bunsen burner was configured to produce a clean-burning, stable flame to minimize flame structure motion and imaging of other radicals. This experiment is intended to validate the capability of ACMIS to perform filtered imaging in a bench top setting. Future development is intended to refine the ACMIS assembly to capture chemiluminescence images

in the combustor of a high-speed wind tunnel to help characterize performance and flame burn characteristics.

Chapter 5

Results and Discussion

The development and characterization of ACMIS produced encouraging results. Data is presented for ACMIS coolant and environment temperatures over the course of extended duration preliminary and extreme thermal cycling experiments. Thermal management capabilities and experimental considerations of the system are discussed. Optically-filtered images of a methane flame are presented as a foundation for development of a chemiluminescence imaging system. Analysis of the data collected in these experiments and continued developments of ACMIS can help advance small-scale imaging system capabilities for high-speed flow applications in harsh thermal environments.

5.1 Preliminary Thermal Cycling

The prototype ACMIS configuration was evaluated by performing five consecutive experiments to analyze the effect of flow rate on the thermal management of the housing. Figure 5.1 depicts the coolant temperatures inside of the prototype CISH recorded by a thermal diode near the image sensor. The results display five independent 90-minute experiments to evaluate the effect of flow rate on the cooling capability of the prototype ACMIS. These flow rates were determined by five preset speeds from an aquarium pump used for the prototype CLCS.

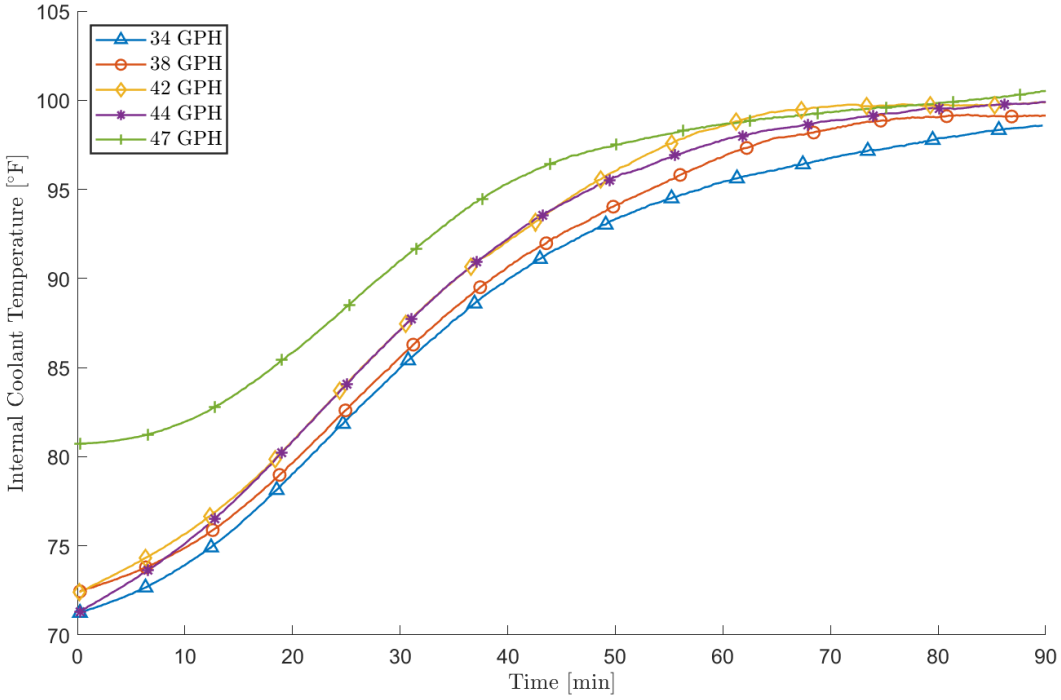

Figure 5.1: Coolant temperature for each pump flow rate (Oven Set Point: 600°F). Note: Highest flow rate experiment was initiated before the environmental test chamber was fully cooled to ambient conditions.

The thermal test chamber was configured to provide an internal environment of 600°F. experiments, For each experiment, the coolant consistently rose by 25-30°F over the course of a 90-minute period before reaching steady state temperatures. The 47 GPH flow rate experiment was initiated before the thermal test chamber was fully cooled to room temperature. This resulted in a higher initial coolant temperature for that run.

An additional control experiment (Figure 5.2) was conducted without the flow of coolant to validate the necessity of coolant flow for successful operation of the camera module. The prototype ACMIS was exposed to 600°F thermal chamber temperatures over the course of two 30-minute experiments, one with coolant flowing (blue data points), and one with the absence of coolant (red data points).

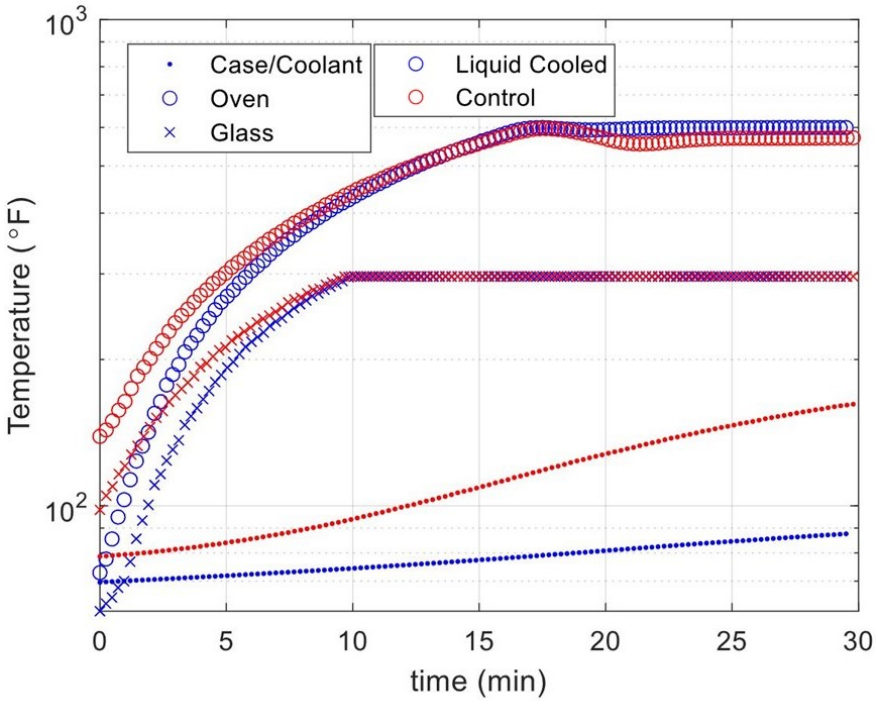

Figure 5.2: Coolant, oven, and window temperatures (log-plot) over a 30-minute test (Oven Set Point: 600°F). Note: the window (glass) thermal diode tops out at 300°F

The oven ramped up to the 600°F set point during the first 15 minutes, followed by consistent 600°F exposure for the following 15 minutes of each experiment. The glass thermal diode tops out at 300°F, so it was not able to continue gathering data above that temperature. It was observed that the coolant provided an approximate 100°F improvement for the internal CISH temperature at the end of the 30-minute exposure. If these experiments were to be run for the entire 90-minute duration with no coolant, the image sensor would likely fail by exceed the maximum operating temperature.

Although the 47 GPH flow rate experiment was initialized at a higher temperature, the coolant reached a steady state temperature consistent with the other experiments. This observation provides a conclusion that changes in flow rate had little effect on the prototype ACMIS configuration. This is possibly due to stagnation regions behind the PCB that could provide passive cooling as opposed to convective flow across the window face. Because flow rate variations had little effect on the thermal management, it was determined that the

further flow path improvements inside the CISH could help optimize thermal management at further elevated conditions.

Over the course of the 90-minute experiments, it was shown that the thermally-managed housing was able to provide sufficient cooling to maintain internal conditions well-within the image sensor's optimal operating range. Figure 5.3 compares the thermal test chamber temperature and the internal CISH temperature over the course of 90-minutes of thermal cycling. The coolant reached steady state temperatures around 100°F. With the flow of coolant, the prototype CISH was able to regulate internal conditions to 500°F lower than the thermal test chamber exposure temperature.

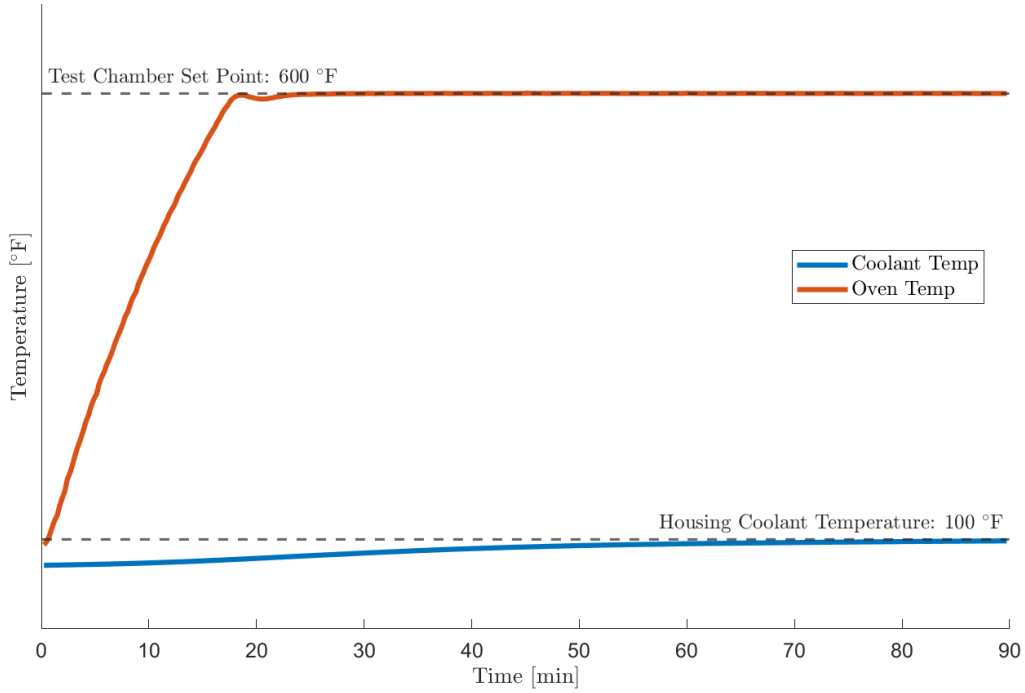

Figure 5.3: Equilibrium conditions of the coolant as the test chamber is heated to and maintained at 600°F

Upgrades to the CLCS with a longer flow path and a higher flow rate pump improved cooling capabilities of the system. The longer flow path provided more surface area for the coolant to transfer heat out of the system. The upgraded pump helped replenish coolant, keeping the camera module environment at lower temperatures than the prototype configuration could achieve. Figure 5.4 depicts the results from the upgraded CLCS preliminary thermal cycling experiment. This plot displays the trends in the thermal test chamber temperature compared to the trends in coolant temperature from the thermal diode, as well as the two Type J thermocouples.

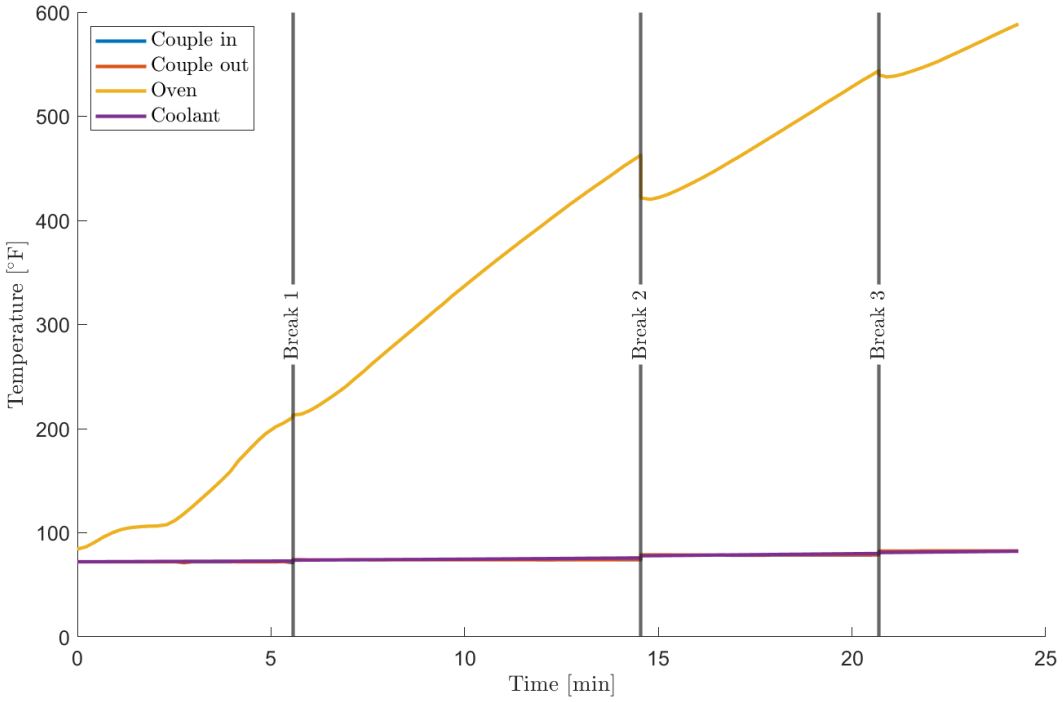

Figure 5.4: Results of preliminary thermal cycling experiment with upgraded CLCS

The upgraded CLCS improved the cooling capability of the ACMIS by approximately 15% based on the temperatures within the CISH at the conclusion of each experiment. Three breaks occurred when performing this experiment. One cause of these breaks was to fix leaks in improperly sealed fittings (Break 1 and Break 3). Another cause of the breaks was due to data transmission issues with the thermocouple data between the 4-channel thermocouple thermometer and the remote workstation. The thermometer continuously outputs temperature data over the RS-232 port based on an internal clock. Whenever an experiment was started, MATLAB would read-in temperature data collected before major temperature ramping, causing the automated test algorithm to see the coolant as having reached equilibrium and proceeding to the next phase of the experiment. This also created a mismatch between visually-inspected temperature values on the thermometer and the live data output from the MATLAB plot, resulting in a manual reset as an attempt to fix this issue (Break 2). The MATLAB buffer issue was addressed for progression to extreme thermal cycling experiments to ensure synchronized data collection during experiments.

After implementation of CLCS improvements, these experiments provided promising results as a basis for more extreme thermal cycling validation. Improvements to the internal flow path in the CISH were made after completing the preliminary thermal cycling experiment to provide more efficient cooling by minimizing stagnation and recirculation regions and ensure proper coolant replenishment throughout the housing.

5.2 Extreme Thermal Cycling

The extreme thermal cycling was conducted in a manner to reflect what the ACMIS would experience in the targeted RC-19 tunnel experiment. With this tunnel configuration, ACMIS would experience long-term idle at 800°F, followed by a short duration combustion period on the order of 30 seconds where the tunnel wall would experience 1,300°F. In order to replicate this, the MF-1000 electric melting furnace was set to higher temperature values so that thermal conditions near the CISH exposed face reached target temperatures.

Figure 5.5 displays the incoming and outgoing coolant temperatures (blue) and window temperatures (orange) over the course of this experiment. Regions during which the furnace was held at set temperatures are shaded. The data is displayed using a fifth-order median filter for data smoothing.

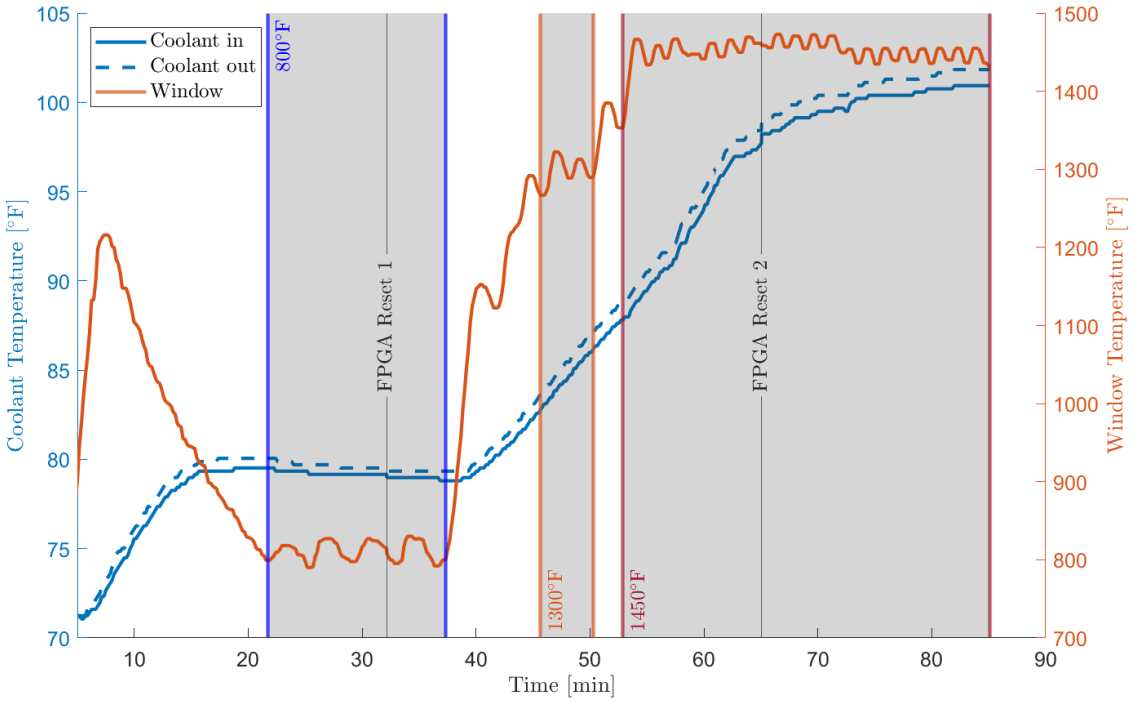

Figure 5.5: Results of ACMIS extreme thermal cycling (fifth-order median filtered)

It was found that the FPGA began to experience a data transmission "bottleneck" after approximately 33 minutes of data collection, and required a reboot after offloading data to be able to continue data collection. This was later found to be due to a limitation with the HDMI academic licence used to provide a camera preview window to a monitor directly from the FPGA. The academic licence is limited to 30 minutes of run time, which caused the FPGA to start sending errors over the USB connection to the MATLAB GUI and flooding the GUI with error messages. This resulted in the MATLAB GUI freezing up after the approximate 33 minute period, requiring an FPGA reboot. Because this experiment was run over the course of an 85-minute period, the FPGA required two reboots during the course of

the experiment, noted in Figure 5.5. Additionally, due to a grounding loop created between the front window thermocouple and the protective melting furnace cage, erroneous readings were being output from the Type K thermocouple much lower than actually experienced. This led to the conclusion that the furnace had to be set much higher to expose ACMIS to the intended conditions. This was quickly noted and fixed by isolating the thermocouple lead from grounding sources, and can be seen by the initial window temperature spike.

Once this issue was realized and fixed, the furnace temperatures were lowered so that the window would experience the intended 800°F conditions. After a 15-minute period, the coolant reached a thermal pseudo-equilibrium, with a gradual decrease in temperature due to the initial furnace set-point overshoot. At this point, the oven was heated such that the exposed CISH adapter and window would experience short-duration thermal conditions at 1,300°F. During this phase, the coolant managed to regulate the thermal conditions around the camera module such that the coolant temperature only increased by 4 degrees Fahrenheit over the course of a 5-minute period. At this point, the wind tunnel application simulation had been completed, and the furnace was heated again to push the system beyond the targeted conditions. This was done in order to stress-test ACMIS to determine coolant equilibrium conditions around a window exposure temperature of 1,450°F, which is just below the 1,500°F corrosion resistance threshold of the stainless steel components used in this work. After a 30-minute period at these elevated conditions, the coolant began to reach steady-state temperatures around 100°F, with a 0.9°F increase in coolant temperature between the incoming and outgoing coolant lines from the CISH.

The thermocouples used in this work have an uncertainty of ±0.18°F (0.1°C). This is a low error for the high temperatures experienced by the Type-K thermocouple exposed to the extreme environment, only producing a 0.01-0.02% measurement uncertainty. At the coolant pseudo-equilibrium temperatures around 100°F, the Type-J thermocouples attached to the CISH produced 0.18% measurement uncertainty.

Additionally, a digital flow meter was used to measure the flow rate produced by the pump, which produced a flow rate of 8 liters per minute, while being run at a lower voltage. The flow meter has an uncertainty of ± 0.4 LPM, resulting in a 5% measurement uncertainty for 8 LPM flow rate.

The melting furnace was not supplied with any illumination. During the course of this experiment, the ceramic lining of the furnace produced ambient illumination due to elevated temperatures of the heating element. Figure 5.6 displays a scaled image captured by ACMIS during the extreme thermal cycling looking down into the melting furnace. The image was captured using a 4.373ms exposure time, which is the maximum exposure timing for the IMX273 sensor using 10-bit ADC. Analog gain of 20dB helped provide more intensity resolution due to low intensity values.

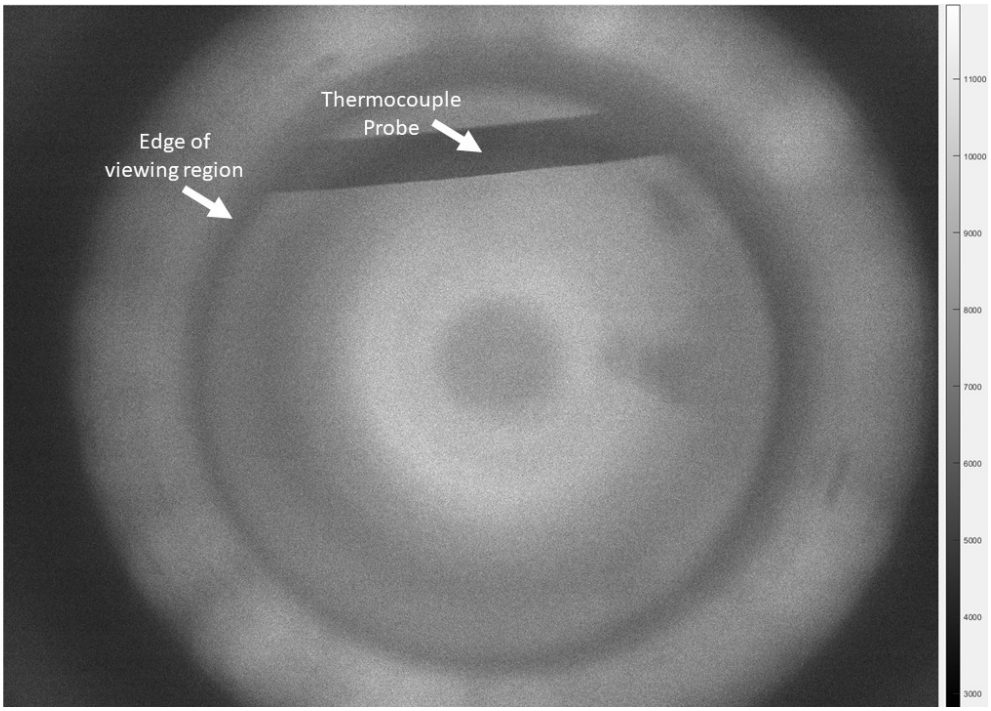

Figure 5.6: Scaled image of MF-1000 ceramic self-illumination at the end of the heating cycle (1,450°F)

This image was captured at the end of the experiment during 1,450°F window exposure when the ceramic material was self-illuminating due to the extreme temperature environment. This provided verification of the location of the Type-K thermocouple near the front of the CISH protective viewing window.

Analysis of the heat removed from the CISH by the FC-72 coolant can be conducted using Equation 2.1. For a coolant flow rate of 8 LPM, the change in temperature across the hot and cold thermocouples can be used to characterize the CISH cooling capabilities at each environmental exposure using FC-72 properties that can be found in the technical documentation [63]. During the 800°F exposure, the coolant temperature increased by 0.54°F (0.3°C) across the coolant lines of the CISH, providing an approximate 74 Watt heat removal rate. During both the 1,300°F and the 1,450°F exposures, the coolant temperature increased by 0.9°F (0.5°C) across the coolant lines of the CISH, providing an approximate 123 Watt heat removal rate.

The cooling capabilities of ACMIS could be further improved by implementation of a chilling system for the FC-72 in the CLCS before entering the CISH. Future improvements to ACMIS could enable even higher temperature operation for analysis of an even broader range of wind tunnels and scramjet models with more extended duration exposure.

5.3 Chemiluminescence Imaging Application

After validation of the cooling capabilities of the ACMIS, the CISH was configured in a horizontal orientation to view a Bunsen burner flame using 430nm and 520nm optical filters to capture spectrally-resolved images for visualization of radical formation based on light emission. Figure 5.7 depicts scaled, optically filtered images of the Bunsen burner flame. These images were cropped to the relevant flame features.

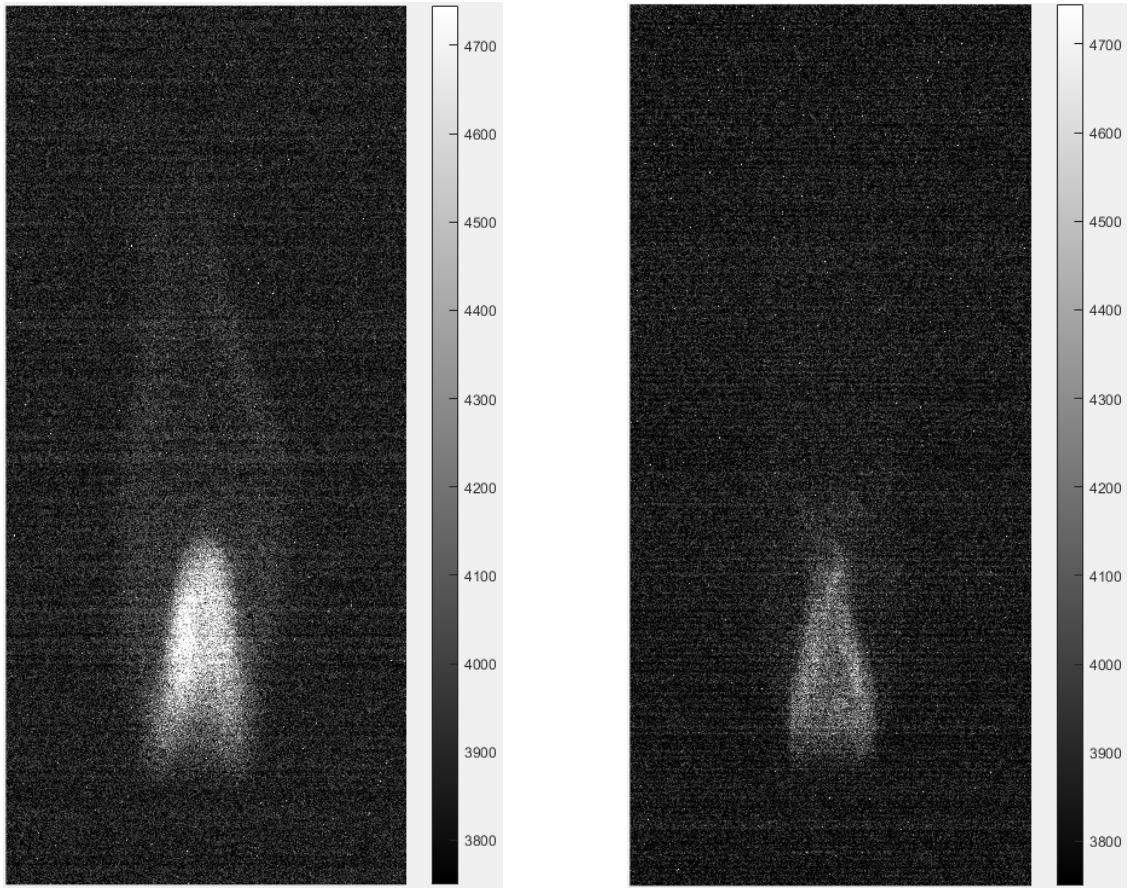

(a) (b)

Figure 5.7: Scaled grayscale images (cropped) of Bunsen burner flame using: (a) 430nm wavelength filter, (b) 520nm wavelength filter

These images were captured using a 4.373ms exposure time, which is the maximum exposure timing for the IMX273 sensor using 10-bit ADC. Analog gain of 20dB helped provide more intensity resolution due to low intensity values. By scaling these images across the minimum and maximum pixel intensities, more flame structure detail is revealed. By time averaging a series of 50 images of the flame using each filter, image noise can be reduced. Figure 5.8 displays time-averaged image series of the Bunsen burner flame for each filter.

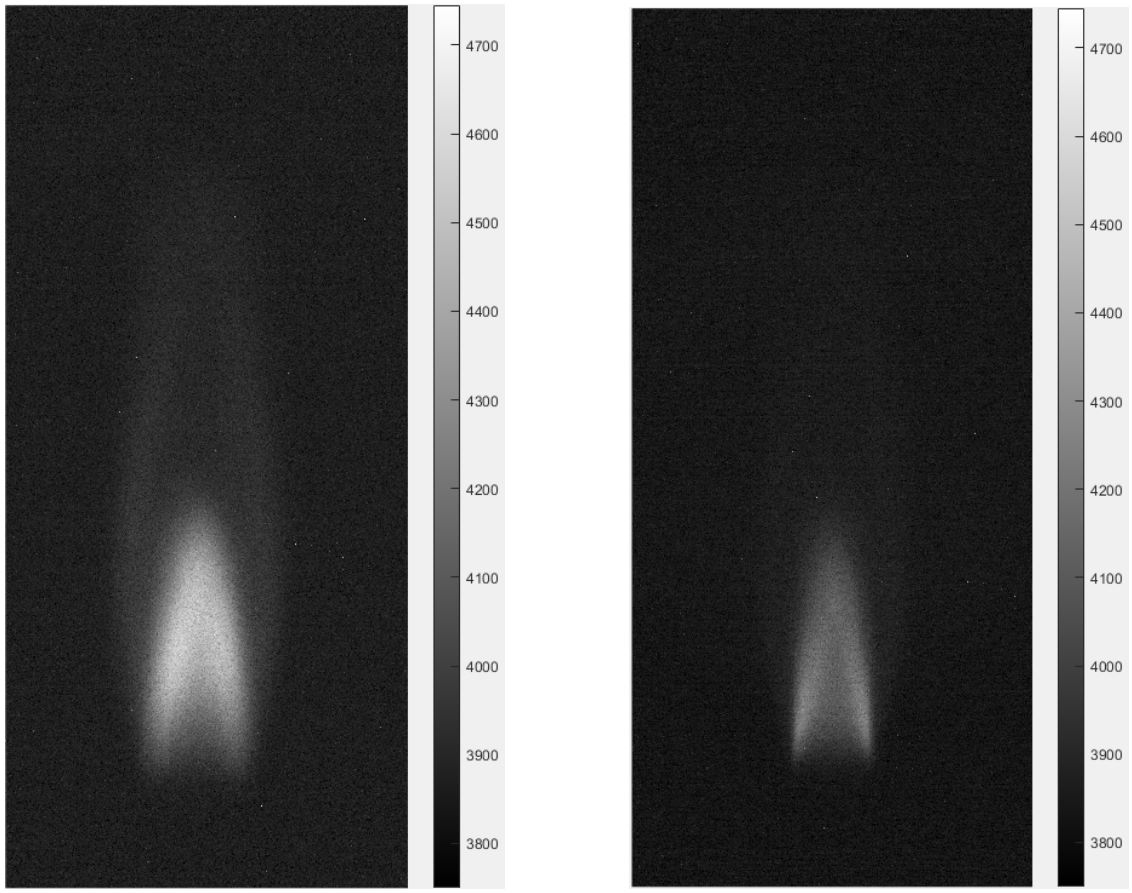

(a) (b)

Figure 5.8: Time-averaged scaled images of Bunsen burner flame using: (a) 430nm wavelength filter, (b) 520nm wavelength filter

From Figure 5.8, it can be seen that 430 nm emissions occur intensely in the core of the flame as well as near the edges of the outer diffusion cone. Emissions at 520 nm primarily occur in the core of the flame. This highlights reaction regions with high localized temperatures. Illumination near the base edges of the flame front is consistent with filtered results of other studies that observe chemiluminescence of methane flames [25].

This experiment successfully validated the capability of ACMIS to capture bandpass-filtered images for chemiluminescence imaging using FC-72 coolant as a medium between optical components. Although these scaled images have low intensities, the Bunsen burner flame imaged was a relatively low-light flame. Wind tunnel facilities with combustion regions or flame holders would have a much higher intensity burn to provide more illumination to

the sensor. A benefit of using the IMX273 monochromatic image sensor is that the exposure timing can be decreased in the case of high illumination levels.

Further refinement of this assembly, as well as the use of additional bandpass filters could enable the use of image processing algorithms, such as the four-line processing method used with a variety of chemiluminescence studies [25, 33, 34], to be able to isolate CH^* and C_2^* radical emissions from background emissions that are included in the images in Figure 5.8. Four-line image processing would provide the capability to measure flame properties such as the overall fuel-to-air ratio and local equivalence ratio in premixed flames using the intensity ratio of C_2^*/CH^*.

Chapter 6

Conclusion

In conclusion, the development of the actively-cooled miniature imaging system (ACMIS) showcases the potential of small board-mounted CMOS image sensors for aerospace optical measurements in extreme temperature environments. The system's small footprint presents potential opportunities to embed image sensors into a variety of aerospace test articles and vehicles for novel flow measurements difficult to capture with traditional imaging systems.

The small package size of the cooled image sensor housing provides the ability for this system to be incorporated into a variety of high temperature wind tunnel experiments, removing the need for large-scale windows for exterior optical access.

The successful maintenance of internal temperatures at 100°F for extended duration exposure at 1,450°F demonstrated the robustness of the system. One consideration of the design presented in this work is that the melting furnace only exposes a small region in front of the CISH to extreme thermal environments. Additionally the front adapter has a small footprint, providing additional nearby surface areas for heat to radiate away from the system. The intended wind tunnel application in the WPAFB Supersonic Research Facility (RC-19) would have a much larger adapter component with a larger surface area exposed to extreme environments that would absorb and store a greater amount of heat energy. In light of this, although a tunnel experiment would expose ACMIS to extended duration conditions around 800°F, ACMIS would only experience a short duration exposure (on the order of 30 seconds) to the 1,300°F combustion environment, providing confidence for system integration in a wind tunnel environment.

Moreover, flow path optimization and addition of a radiator or an industrial chiller system to actively cool the FC-72 fluid before entering the CISH open avenues for refining the

cooling capabilities of ACMIS. Further improvements to the CLCS to provide robust sealing could enable even higher flow rates to improve the circulation of fresh coolant. Application of a spray-on thermal barrier coating (TBC) or addition of a ceramic liner between the CISH and a tunnel wall could further refine system performance by adding significant insulation to the front of the housing. Testing of different coolants with ACMIS could reduce system costs and provide additional cooling capabilities. Addition of a safety bypass loop to evacuate coolant in the event of pump failure or high coolant temperatures can increase system safety for application in wind tunnel environments, where fume hood ventilation would not always be readily available.

This work also incorporated integrated optical filters, providing the ability to capture spectrally-resolved images and potential advancements in combustion flame chemiluminescence imaging. With further system refinement and development of a four-line image processing algorithm, optically-filtered ACMIS images could be processed to isolate individual radicals to determine flame structure based on emission locations as well as the equivalence ratio for premixed flames by comparison of CH^* and C_2^* emission. Additional optical filters offset from the bandpass filters used in this study can be implemented to identify emission from other radicals, especially broadband emission of CO_2^*, in order to isolate emission from relevant radicals.

This work helps lay a foundation for embedded imaging research in high-enthalpy tunnel environments, emphasizing the cost-effectiveness and adaptability of small form factor sensors to image constrained flows. The low costs and wide availability of COTS hardware enables short-term or single-use imaging applications of this system. ACMIS presents a novel solution for internal flow measurements in high enthalpy flows by implementing active immersion cooling with inexpensive hardware components that can observe regions that have traditionally been hard to observe and measure. With further development, ACMIS has the potential to be adapted as an inexpensive, lightweight system for future applications in flight experiments with harsh thermal environments.

Bibliography

[1] Smart, M. K., "Scramjet Inlets," 2010.

[2] Gu, S., and Olivier, H., "Capabilities and limitations of existing hypersonic facilities," *Progress in Aerospace Sciences*, Vol. 113, 2020.

[3] Gruber, M. R., and Nejad, A. S., "New supersonic combustion research facility," *Journal of Propulsion and Power*, Vol. 11, No. 5, 1995, pp. 1080–1083.

[4] Ombrello, T., Carter, C., Mccall, J., Schauer, F., Tam, C.-J., Taitech, A., Naples, Hoke, J., and Hsu, K.-Y., "Pulsed Detonation Combustor in a Supersonic Cross-Flow for Enhanced Mixing and Ignition," 2011.

[5] Garrard, G. D., *Hypersonic Test Capabilities at AEDC's Aerodynamic and Propulsion Test Unit*, 2015.

[6] Lafferty, J. F., Coblish, J. J., Marineau, E., Norris, J. D., Kurits, I., Lewis, D. R., Smith, M., and Marana, M., *The Hypervelocity Wind Tunnel No. 9; Continued Excellence Through Improvement and Modernization*, 2015.

[7] Kidd, F. G., Narayanaswamy, V., Danehy, P. M., Inman, J. A., Bathel, B. F., Cabell, K. F., Hass, N., Capriotti, D., Drozda, T. G., and Johansen, C. T., *Characterization of the NASA Langley Arc Heated Scramjet Test Facility using NO PLIF*, 2014.

[8] Kreth, P. A., Gragston, M., Davenport, K., and Schmisseur, J. D., *Design and Initial Characterization of the UTSI Mach 4 Ludwieg Tube*, 2021.

[9] Bakos, R. J., Tsai, C., Rogers, R. C., and Shih, A. T., "The Mach 10 Component of NASA's Hyper-X Ground Test Program," 1999.

[10] Baccarella, D., Liu, Q., McGann, B., Lee, G., and Lee, T., "Isolator-combustor interactions in a circular model scramjet with thermal and non-thermal choking-induced unstart," *Journal of Fluid Mechanics*, Vol. 917, 2021.

[11] Eagan, G. D., Lewis, C. J., Alles, R. M., Klingaman, K. C., Davenport, K., Gragston, M. T., Rice, B. E., Hamilton, M. C., and Thurow, B. S., "Direct Measurements of Shock Impingement in a Busemann Inlet via a Miniature Embedded Imaging System," *AIAA SCITECH 2023 Forum*, 2023.

[12] Pandey, A., Schmidt, B. E., and Casper, K. M., *Demonstration of Internal-Digital Image Correlation for Fluid-Structure Interaction Measurements in a Hypersonic Wind Tunnel*, 2022.

[13] "VC MIPI Camera Module Hardware Operating Manual," 2023.

[14] AMD, "Zynq UltraScale+ MPSoC ZCU106 Evaluation Kit," 2023.

[15] "Lightweight Thermal Protection System for Hypersonic Aerial Vehicles," 2021, N211-016.

[16] Yancey, R., "Meeting the High-Temperature Material Challenges of Hypersonic Flight Systems," 2021.

[17] Liu, D. S.-K., *Numerical Simulation of Hypersonic Aerodynamics and the Computational Needs for the Design of an Aerospace Plane*, RAND Corporation, Santa Monica, CA, 1992.

[18] Förster, F. J., Dröske, N. C., Bühler, M. N., von Wolfersdorf, J., and Weigand, B., "Analysis of flame characteristics in a scramjet combustor with staged fuel injection using common path focusing schlieren and flame visualization," *Combustion and Flame*, Vol. 168, 2016, pp. 204–215.

[19] Li, L. Tian, Y. Deng, X. Guo, M. Le, J. and Zhang, H. "Segmentation of schlieren images of flow field in combustor of scramjet based on improved fully convolutional network," *Physics of Fluids*, Vol. 34, No. 11, 2022.

[20] Watanabe, S., "Scramjet nozzle experiment with hypersonic external flow," *Journal of Propulsion and Power*, Vol. 9, No. 4, 1993, pp. 521–528.

[21] Hsu, K.-Y., Carter, C. D., Gruber, M. R., Barhorst, T., and Smith, S., "Experimental Study of Cavity-Strut Combustion in Supersonic Flow," *Journal of Propulsion and Power*, Vol. 26, No. 6, 2010, pp. 1237–1246.

[22] Eagan, G., Lewis, C., Alles, R., Rice, B., Hamilton, M., and Thurow, B., "Development of a Miniature Embedded Imaging System for Internal Flow Measurements," *20th International Symposium on Application of Laser and Imaging Techniques to Fluid Mechanics*, 2022.

[23] Yue, L.-J., Chen, L.-H., Xiao, Y.-B., Gong, P., and Chang, X.-Y., *Research on Three-Dimensional Scramjet Inlet*, 2012.

[24] Tinaut, F., Reyes, M., Gimenez, B., and Pastor, J., "Measurements of OH* and CH* Chemiluminescence in Premixed Flames in a Constant Volume Combustion Bomb under Autoignition Conditions," *Energy & Fuels*, Vol. 25, 2010.

[25] Liu, Y., Tan, J., Wan, M., Zhang, L., and Yao, X., "Quantitative Measurement of OH* and CH* Chemiluminescence in Jet Diffusion Flames," *ACS Omega*, Vol. 5, No. 26, 2020, p. 15922—15930.

[26] Huang, H. W., and Zhang, Y., "Digital colour image processing based measurement of premixed CH_4 + air and C_2H_4 + air flame chemiluminescence," *Fuel*, Vol. 90, No. 1, 2011, pp. 48–53.

[27] Elkowitz, L., Goyne, C. P., and Dedic, C. E., "Flame Chemiluminescence Sensing and Analysis for Scramjet Control," *Optical Sensors and Sensing Congress 2022 (AIS, LACSEA, Sensors, ES)*, Optica Publishing Group, 2022.

[28] Ballance, H. C., Bibik, O., Cook, T. S., Danczyk, S., Schumaker, S. A., and Lieuwen, T., *High Speed Optical Diagnostics in a High Pressure, RP-2/GOx Fueled Combustor*, 2017.

[29] Gaetano, A. R., Pritschau, T. C., Betancourt, J. J., Shaw, V. G., Wiggins, R., and Gutmark, E. J., "Comparative Analysis of Broadband Imaging and CH* Chemiluminescence for Ascertaining Modal Operation in a Rotating Detonation Combustor," Jan. 2022.

[30] Tonarely, M. E., Genova, T., Morales, A. J., Micka, D., Knaus, D., and Ahmed, K. A., "Four-Line C2*/CH* Optical Sensor for Chemiluminescence Based Imaging of Flame Stoichiometry," *Sensors*, Vol. 22, No. 15, 2022.

[31] Panoutsos, C., Hardalupas, Y., and Taylor, A., "Numerical evaluation of equivalence ratio measurement using OH and CH chemiluminescence in premixed and non-premixed methane–air flames," *Combustion and Flame*, Vol. 156, No. 2, 2009, pp. 273–291.

[32] Reyes, J., Kailasanathan, R. K. A., and Ahmed, K., "Relationship between the Chemiluminescence Intensity Ratio of C2* and CH*, Charge Pressure, and Equivalence Ratio for Gasoline," *Energy & Fuels*, Vol. 32, No. 10, 2018, pp. 10933–10940.

[33] Karnani, S., and Dunn-Rankin, D., "Visualizing CH* chemiluminescence in sooting flames," *Combustion and Flame*, Vol. 160, No. 10, 2013, pp. 2275–2278.

[34] Tonarely, M., Genova, T., Morales, A., Micka, D., Knaus, D., and Ahmed, K., "Four-Line C2*/CH* Optical Sensor for Chemiluminescence Based Imaging of Flame Stoichiometry," *Sensors*, Vol. 22, 2022.

[35] Heiser, W., Pratt, D., Daley, D., and Mehta, U., *Hypersonic Airbreathing Propulsion*, American Institute of Aeronautics and Astronautics, Inc., 1994.

[36] Segal, C., *The Scramjet Engine: Processes and Characteristics*, Cambridge Aerospace Series, Cambridge University Press, 2009.

[37] Mills, M., *Hypersonic Test Capabilities in Tunnels B and C at AEDC's von Karman Facility*, 2015.

[38] "Supersonic Research Facility (Research Cell 19)," 2020.

[39] Lu, F. K., and Marren, D. E., *Principles of Hypersonic Test Facility Development*, 2002, pp. 17–27.

[40] Mamplata, C., and Tang, M., *Technical Approach To Turbine-Based Combined Cycle: FaCET*, 2009.

[41] Metzger, M. A., "Graphite Heating Element Operating Temperature Measurements in the NSWC Hypervelocity Wind Tunnel 9," 1997.

[42] Dogariu, A., Dogariu, L. E., Smith, M. S., McManamen, B., Lafferty, J. F., and Miles, R. B., *Velocity and Temperature Measurements in Mach 18 Nitrogen Flow at Tunnel 9*, 2021.

[43] Marren, D., "Aero-Optical Demonstration Test in the AEDC Hypervelocity Wind Tunnel 9," 1999.

[44] Hass, N. E., and Cabell, K. F., "Current Test Capabilities of NASA Langley's Arc-Heated Scramjet Test Facility," Joint Army-Navy-NASA-Air Force (JANNAF) Meeting, 2020.

[45] Li, Z., Xiong, Y., Yuan, X., Chen, J., Zhao, J., and Wu, J., "A-Variant Design of Hypersonic Ludwieg Tube Wind Tunnel," *AIAA Journal*, Vol. 60, No. 7, 2022, pp. 3990–4005.

[46] Smith, C. D., Kreth, P. A., Schmisseur, J. D., and Strickland, G., *Temperature-Sensitive Paint Measurements of Cylinder-Induced Shockwave-Boundary Layer Interaction on a 6-degree Cone with Laminar Mach 7 Flow*, 2023.

[47] Maclean, M., Wadhams, T. P., and Holden, M. S., "Integration of CFD and Experiments in the CUBRC LENS Shock Tunnel Facilities to Understand the Physics of Hypersonic and Hypervelocity Flows," 2009.

[48] Wadhams, T., MacLean, M., Holden, M., and Barry, S., *A Review of Transition Studies on Full- Scale Flight Vehicles at Duplicated Flight Conditions in the LENS Tunnels and Comparisons with Prediction Methods and Flight Measurement*, 2010.

[49] Li, Q., Han, A., Yang, G., Hong, Y., Zhang, Z., Jin, L., and Yang, J., "Technical challenges and novel passive cooling technologies for ultra-thin notebooks," *2017 16th IEEE Intersociety Conference on Thermal and Thermomechanical Phenomena in Electronic Systems (ITherm)*, 2017, pp. 1069–1074.

[50] Wagner, G., and Maltz, W., "Thermal management challenges in the passive cooling of handheld devices," *19th International Workshop on Thermal Investigations of ICs and Systems (THERMINIC)*, 2013, pp. 344–347.

[51] Beresh, S. J., Casper, K. M., Wagner, J. L., Henfling, J., Spillers, R., and Pruett, B. O., *Modernization of Sandia's Hypersonic Wind Tunnel*, 2015.

[52] Muneeshwaran, M., Lin, Y.-C., and Wang, C.-C., "Performance analysis of single-phase immersion cooling system of data center using FC-40 dielectric fluid," *International Communications in Heat and Mass Transfer*, Vol. 145, 2023.

[53] Kuncoro, I. W., Pambudi, N. A., Biddinika, M. K., and Budiyanto, C. W., "Optimization of immersion cooling performance using the Taguchi Method," *Case Studies in Thermal Engineering*, Vol. 21, 2020, p. 100729.

[54] Jimenez, P. E., and Mudawar, I., "A Multi-Kilowatt Immersion-Cooled Standard Electronic Clamshell Module for Future Aircraft Avionics," *Journal of Electronic Packaging*, Vol. 116, No. 3, 1994, pp. 220–229.

[55] Brouwer, K. R., Perez, R. A., Beberniss, T. J., Spottswood, S. M., and Ehrhardt, D. A., "Experiments on a Thin Panel Excited by Turbulent Flow and Shock/Boundary-Layer Interactions," *AIAA Journal*, Vol. 59, No. 7, 2021, pp. 2737–2752.

[56] S, V., and Muruganandam, T., "Visualization of over-expanded supersonic wall-jet," *Aerospace Science and Technology*, Vol. 112, 2021.

[57] Glasgow, B., and Bell, W., "The future of anti-aircraft imaging infrared seeker missile threats," *1999 IEEE Aerospace Conference Proceedings (Cat. No.99TH8403)*, Vol. 4, 1999, pp. 457–465.

[58] Wytrykus, F., and Duesterwald, R., "Improving Combustion Process by Using a High Speed UV-Sensitive Camera," *SAE Transactions*, Vol. 110, 2001, pp. 731–738.

[59] Winkleman, B., Scott, K., Beitel, G. R., VanPelt, T. B., Weaver, B., and Conner, M. S., *Application of Stereoscopic Imaging in Aerospace Ground Testing*, 2014.

[60] Beitel, G., Catalano, D., and Edwards, R., *Electroformed Diagnostic Probes for High-Temperature Gas Flows*, 2004.

[61] Hiers, R., and Hiers, R., *Development of High Temperature Image Probes for Viewing Turbine Engine Augmentors*, 2002.

[62] Rosato, D. A., Thornton, M., Sosa, J., Bachman, C., Goodwin, G. B., and Ahmed, K. A., "Stabilized detonation for hypersonic propulsion," *Proceedings of the National Academy of Sciences*, Vol. 118, No. 20, May 2021.

[63] 3M, "3M™ Fluorinert™ Electronic Liquid FC-72," 98-0212-2308-0 datasheet, Sep. 2019.

[64] *3M™ Fluorinert™ Electronic Liquid FC-72*, SDS No. 10-3789-4 [Online]; 3M, Oct. 2021.